COLLECTIVE EXCITATIONS IN LAYERED MATERIALS WITH MOMENTUM-RESOLVED ELECTRON ENERGY LOSS SPECTROSCOPY

BY

ANSHUL KOGAR

DISSERTATION

Submitted in partial fulfillment of the requirements
for the degree of Doctor of Philosophy in Physics
in the Graduate College of the
University of Illinois at Urbana-Champaign, 2015

Urbana, Illinois

Doctoral Committee:

Professor S. Lance Cooper, Chair
Professor Peter Abbamonte, Director of Research
Professor Anthony J. Leggett
Professor Jen-Chieh Peng

Abstract

Strong Coulomb interactions are either suspected or known to play a prominent role in material classes such as high temperature superconductors, charge density waves, and Mott insulators among many others. These interactions are quantified by the charge density response function, $\chi(\mathbf{q},\omega)$ (or the closely related inverse dielectric function). The measurement of the energy- and momentum-resolved $\chi(\mathbf{q},\omega)$ over a large phase space of $\mathbf{q}$ and ω, however, presents a significant experimental challenge. Traditional methods to measure $\chi(\mathbf{q},\omega)$ have suffered from either one or more major drawbacks. To address this problem, the development of a spectroscopic technique, momentum-resolved electron energy loss spectroscopy (M-EELS), was undertaken. Because many of the material classes that exhibit these unusual ground states tend to be layered or quasi-two dimensional, M-EELS presents a promising approach to measuring the energy- and momentum-resolved charge density response. Since the technique is not widely used, however, the M-EELS results obtained as part of this thesis were compared to other probes in the relevant ranges of phase space to ensure consistency. Furthermore, a theoretical framework was worked out to demonstrate explicitly the relationship between the scattering cross section and $\chi(\mathbf{q},\omega)$. M-EELS experiments were conducted on a high-temperature superconductor, $Bi_2Sr_2CaCu_2O_{8+\delta}$, a charge density wave material, $TiSe_2$, and a topological insulator, Bi_2Se_3. It was determined that the bosonic origin of quasiparticle kinks often seen in angle-resolved photoemission studies can be identified using M-EELS. Lastly, the observation of a novel electronic collective mode in $TiSe_2$ is presented as strong evidence for an excitonic insulator phase in this compound.

"A poem is never finished, only abandoned."

- Paul Valery

Acknowledgments

It is difficult to find the words to adequately describe the relationship a student has with his/her advisor because of the extent to which the advisor shapes the student's scientific outlook. I would like to sincerely thank Peter Abbamonte for his guidance, imagination, and confidence in my ability (especially when I lacked the confidence myself). I would also like to thank Lance Cooper, Greg MacDougall, Tai-Chang Chiang, JC Peng and Tony Leggett for sharing many insights and asking probing questions that have helped me formulate a more consistent outlook on many aspects of solids. I would also like to thank my many collaborators whose data collection and theoretical work have made much of my work intelligible.

My lab-mates, Gan, James, Jeremy, Xiao and Young have spent innumerable hours helping me to untie the many mental knots that inevitably arise in studying physics. For this, I thank them greatly. Much of the EELS work undertaken in this thesis would not have been possible without the talent and know-how of Sean Vig and Luc Venema – to them I owe some of the largest thanks. To Mindy and Ali: your excellent questions and company in the lab has been a delight and I wish you the best in the years to come. To Gilberto, Anna and Sangjun: it can no longer be me who has "borrowed" your equipment.

To my friends and colleagues: I have probably learned more about physics (and other topics) at lunch and during chats in your respective offices than I have anywhere else in graduate school. Hopefully, the face-stuffing and debates will continue. To the MRL staff, especially Mauro, Julio, Ernie and Jim: thanks for getting me up to speed when I

was learning the ropes and for your sustained company throughout.

I thank my in-laws, who housed me, fed me and kept me sane during the writing of this thesis. I would also like to thank my own parents – it is almost a tautology to say that this work could not have been done without them, but I continually realize the extent to which they are the giants upon whose shoulders I stand. To Kaushi and Granny: thank you for your love and support. I rarely succeed in expressing my emotions adequately, but I wish that you weren't so far away.

To Niki: I thank you for your support, love, encouragement and companionship. I sense that the road ahead will be paved with bananas, pillows and, undoubtedly, chocolate.

Academic Disclaimer: The author wrote this dissertation in support of requirements for the degree Doctor of Philosophy in Physics at University of Illinois, Urbana-Champaign.

Table of Contents

List of Figures

List of Abbreviations

ARPES	Angle-Resolved Photoemission Spectroscopy
BOA	Born-Oppenheimer Approximation
CCD	Charge-Coupled Device
CDW	Charge Density Wave
COR	Center of Rotation
FT	Fourier Transform
HTS	High-Temperature Superconductor
IEA	Independent Electron Approximation
INS	Inelastic Neutron Scattering
IR	Infrared
IXS	Inelastic Electron Scattering
LEED	Low Energy Electron Diffraction
M-EELS	Momentum-Resolved Electron Energy Loss Spectroscopy
ODLRO	Off-Diagonal Long Range Order
RGA	Residual Gas Analyzer
STM	Scanning Tunneling Microscopy
TMD	Transition Metal Dichalcogenide
UHV	Ultra-High Vacuum

Chapter 1

Introduction

1.1 Generalities

The framework under which solid state physicists work has not changed since the beginning of the field in the 1920s. While philosophies and outlooks have altered markedly, the Hamiltonian has remained the same. This is the Hamiltonian that Laughlin and Pines have called the Theory of Everything (and simultaneously the Theory of Nothing) in a condensed matter setting [4]:

$$i\hbar\frac{\partial}{\partial t}\left|\Psi\right\rangle = H\left|\Psi\right\rangle \tag{1.1}$$

where

$$H = -\sum_{j}^{N_e}\frac{\hbar^2}{2m}\nabla_j^2 - \sum_{\alpha}^{N_i}\frac{\hbar^2}{2M_\alpha}\nabla_\alpha^2 - \sum_{j}^{N_e}\sum_{\alpha}^{N_i}\frac{Z_\alpha e^2}{|\mathbf{r}_j - \mathbf{R}_\alpha|} + \sum_{j<k}^{N_e}\frac{e^2}{|\mathbf{r}_j - \mathbf{r}_k|} + \sum_{\alpha<\beta}^{N_i}\frac{Z_\alpha Z_\beta e^2}{|\mathbf{R}_\alpha - \mathbf{r}_\beta|}. \tag{1.2}$$

The symbols Z_α and M_α are the atomic number and the mass of the α^{th} nucleus, R_α is the location of the nucleus, e and m are the electron charge and mass, r_j is the location of the j^{th} electron and $\hbar$ is Planck's constant [4].

Since this equation is intractable for almost all problems in solid states physics, however, a number of simplifying assumptions must be made to make this equation soluble. The most commonly used scheme is the Born-Oppenheimer approximation (BOA). The

BOA permits one to decouple the motion of the nuclei and core electrons from the motion of the valence electrons. Once this decoupling has been made, the effective interaction between the valence electrons is no longer the bare Coulomb interaction as in the Eq. 1.2, but a screened Coulomb interaction. The screening comes from the interband contribution of the core electrons. We can therefore write the Hamiltonian of the subsystem consisting of the valence electrons as (up to first order in the coupling between the phonons and electrons):

$$H_e = \sum_j^{N_e} \frac{\mathbf{p}_j^2}{2m} + U(\mathbf{r}_j) + \sum_j^{N_e} \sum_\alpha^{N_i} \mathbf{u}_\alpha \cdot \nabla U_{e-i}(\mathbf{r}_j - \mathbf{R}_\alpha) + \sum_{j<k}^{N_e} V_c(\mathbf{r}_j, \mathbf{r}_k), \tag{1.3}$$

where

$$V_c(\mathbf{r}_j, \mathbf{r}_k) = \frac{e^2}{\epsilon_{sc}|\mathbf{r}_j - \mathbf{r}_k|}, \tag{1.4}$$

$\mathbf{p}_j$ and $\mathbf{r}_j$ are the momentum and position of the j^{th} valence electron, $U(\mathbf{r}_j)$ is the local potential on the valence electrons due to the static periodic field of the lattice, $\mathbf{u}_\alpha \cdot \nabla U_{e-i}(\mathbf{r}_j - \mathbf{R}_\alpha)$ describes the first-order change in the static lattice potential due to lattice vibrations, and $V_c(\mathbf{r}_j, \mathbf{r}_k)$ describes the screened Coulomb interaction between the valence electrons through the dielectric constant, ϵ_{sc}.

The neglect of the last two (electron-phonon and electron-electron) interaction terms in Eq. 1.3 is commonly referred to as the independent electron approximation (IEA) and is the framework which underpins the band theory of solids [5, 6]. Its successes in describing many properties of elemental solids and simple alloys have been well-documented [5, 6]. The failures of this neglect, however, are as spectacular as they are common. For instance, an adequate theory of electron transport in metals must take into consideration the effects of scattering from phonons [6]. In addition, at low temperatures, most solids undergo phase transitions to broken symmetry states that cannot be described without including either one or both of these terms in some capacity [6, 7].

The most important problems in solid state physics today concern effects in which the IEA breaks down leading to the formation of spectacular ground states, such in high-temperature superconductivity and charge density waves. In many of these material classes, it is suspected that there is a prominent role played by both the quasi-two dimensionality and a strong Coulomb interaction present in these materials. It is also suspected that fluctuations of these ground states persist into the normal phase making difficult a complete description of the high temperature phase. Because theoretical formulations of many of the normal state properties has so far eluded theoretical consensus, experimental quantification of Coulomb interactions in these systems is particularly pertinent.

1.2 Quantification of Coulomb Interactions

The physical quantities that parameterize the effective Couloumb interaction between valence electrons in a solid are the charge density response function, $\chi(\mathbf{q},\omega)$ and the closely related inverse longitudinal dielectric function, $1/\epsilon^L(\mathbf{q},\omega)$ [8]. Both of these quantities are wavevector- and frequency-dependent and are also complex quantities. A simple argument demonstrates the significance of the inverse dielectric function. Starting from the Fourier-transformed Maxwell equations under the assumption of translational invariance, one can write (in the Coulomb gauge where $\mathbf{q}\cdot\mathbf{A}(\mathbf{q},\omega)=0$):

$$i\mathbf{q}\cdot\mathbf{D}^L(\mathbf{q},\omega) = 4\pi\rho_{ext} \tag{1.5}$$

$$i\mathbf{q}\cdot\mathbf{E}^L(\mathbf{q},\omega) = 4\pi\rho_{tot} = 4\pi(\rho_{ind}+\rho_{ext}) \tag{1.6}$$

$$\mathbf{D}^L(\mathbf{q},\omega) = -i\mathbf{q}\phi_{ext}(\mathbf{q},\omega) \tag{1.7}$$

$$\mathbf{E}^L(\mathbf{q},\omega) = -i\mathbf{q}\phi(\mathbf{q},\omega) \tag{1.8}$$

$$\phi(\mathbf{q},\omega) = \frac{\phi_{ext}(\mathbf{q},\omega)}{\epsilon^L(\mathbf{q},\omega)}, \tag{1.9}$$

where ρ_{ext}, ρ_{ind} and ρ_{tot} are the external, induced and total charge density respectively, and ϕ are the corresponding scalar potentials. Eq. 1.9 shows that if one wishes to characterize the effect of the Coulomb interactions in a solid, the inverse longitudinal dielectric function is the pre-eminent parameter. From the equations above, one can see that: (1) the real part of the inverse dielectric function determines the effective Coulomb interaction and (2) the imaginary part of the inverse dielectric function will peak at collective modes that mediate the interactions between the valence electrons. The second point here is a little more difficult to see immediately, but will be further elaborated upon in the theoretical section of this thesis. Lastly, for a translationally invariant system, the inverse longitudinal dielectric function is related to $\chi(\mathbf{q},\omega)$like so:

$$\frac{1}{\epsilon^L(\mathbf{q},\omega)} = 1 + V(\mathbf{q})\chi(\mathbf{q},\omega), \tag{1.10}$$

where

$$V(\mathbf{q}) = \frac{4\pi e^2}{\mathbf{q}^2}, \tag{1.11}$$

demonstrating that the quantities contain identical physical information.

1.3 Measurement Techniques

The measurement of the momentum- and energy-resolved inverse longitudinal dielectric function or the charge density response function presents a significant experimental challenge. There are few existing probes that can measure the inverse dielectric function with high resolution over the entire Brillouin zone. The currently most widely used probes for measuring the density correlations are the following: (1) Inelastic X-ray Scattering (IXS), (2) Infrared Spectroscopy (IR), (3) Ellipsometry, (4) Raman Spectroscopy, (5) Resonant Inelastic X-ray Scattering (RIXS) and (6) Transmission Electron Energy Loss Spectroscopy (T-EELS). All of these techniques suffer from one or more major drawbacks that impedes

these techniques from being able to access the density correlations with high energy resolution and over a large swathe of the Brillouin zone in the materials of interest here.

The techniques that use visible or infrared light to probe solids (IR, Raman and Ellipsometry) are confined to looking at regions of momentum space close the the Brillouin zone center. This is a fundamental obstacle due to the wavelength of the incident radiation that cannot be overcome. However, these studies are of the highest energy resolution and are extremely valuable in probing zone center excitations. IXS also suffers from an inherent shortcoming: since X-rays probe the *electron* density and not the *charge* density, IXS is necessarily partial to studying lattice vibrations instead of electronic excitations. Furthermore, as one increases the atomic number, the absorption cross section scales as Z^4, leaving one with an extremely low count rate, rendering unrealistic the possibility of obtaining spectra on a reasonable time-scale [9]. Of these probes, T-EELS is the only one that is constrained by a technological, as opposed to an inherent, obstacle. At the present time, T-EELS suffers from poor energy resolution, but rapid advances in electron optics by the transmission electron microscopy community suggests that this is a temporary impediment [10, 11]. These deficiencies are summarized in the table below.

Method	**Drawback**
X-rays (IXS)	Absorption Cross Section $\propto Z^4$; Partial to Core Electrons
Infrared Spectroscopy (IR)	$\mathbf{q} = 0$; Requires Kramers-Kronig
Ellipsometry	$\mathbf{q} = 0$
Raman Spectroscopy	$\mathbf{q} = 0$; Relationship to $\chi(\mathbf{q}, \omega)$not clear
Resonant X-rays (RIXS)	$\sim$50-100 meV energy resolution; Relationship to $\chi(\mathbf{q}, \omega)$not clear
Transmission EELS (T-EELS)	$\sim$50-100 meV energy resolution

Table 1.1: Problems with current probes of charge density correlations

Momentum-resolved electron energy loss spectroscopy (M-EELS), presents a possible solution to this problem, especially for a number of the aforementioned material classes. M-EELS is an inelastic electron scattering technique that uses low energy electrons to

scatter off charge density excitations from the solid surface of interest. Because of the low energy of the incoming electrons, much better energy resolution ($\sim$1-2 meV) than T-EELS can be obtained. The relationship between the solid surface and the bulk properties of the material are not necessarily simple, however. Comparisons with other probes at relevant momenta, such as infrared spectroscopy, therefore give one insight into how much bulk information can be determined from this surface-sensitive probe. In this thesis, M-EELS studies were undertaken for a high-temperature superconductor, a topological insulator and a charge density wave system with the intention of understanding better: (1) the capabilities of the newly developed probe, (2) the sensitivity of the probe to bulk excitation versus surface excitations and (3) the electron-electron interactions in the materials investigated.

1.4 Specific Questions

In the literature, there have been repeated calls for the inverse dielectric function or the charge density response function to be measured in different contexts [12–18]. These contexts include, but are not limited to, the aforementioned material classes: charge density wave systems, high-temperature superconductors, and topological insulators.

While there are many reasons for these calls, they are in part due to the likely existence of low-energy electronic collective excitations that have, as yet, been unobserved. These occur even in familiar material classes, some of which have been studied for decades. Their existence is evidenced by the appearance of quasiparticle dispersion kinks, observed with angle-resolved photoemission spectroscopy (ARPES), that sometimes occur on energy scales higher than usual phonon energy scales [13, 19–21]. Because of this, their origin is hotly debated and speculated upon. However, because ARPES probes the fermionic quasiparticles, it is an extremely indirect way to measure the bosonic collective modes. Undoubtedly, it would be more effective to measure these electronic collective

modes by measuring the charge density response function.

Another important reason to measure the inverse dielectric function has been stressed by Leggett that could have important implications for cuprate superconductors [14, 15]. He suggests that a measurement of the momentum-dependent inverse dielectric function could demonstrate that the reduction in energy associated with the superconducting transition results from a lowering of the Coulomb energy. In particular, this scenario leads one to examine the mid-infrared peak, a generic property of high-temperature superconductors, where the reduction in energy is expected to occur. This peak, observed in previous studies using transmission EELS, has not been systematically studied as a function of $\mathbf{q}$ and temperature.

Furthermore, there has been a lively recent debate in the literature concerning the origin of charge density waves in several layered compounds including the TMDs [12, 22–25]. Fermi surface nesting has historically been argued to be the origin of charge density waves in the transition metal dichalcogenides [7, 26]. However, this viewpoint has been challenged recently, and the measurement of the real part of the charge density response function has been pinpointed as a resolution to some of these issues [12]. For these systems, it is also of vast importance to measure the dispersion of the collective modes to be able to understand the role of electron-electron interactions and electron-phonon coupling in the formation of the CDW state [27].

In this thesis, several of these questions will be directly addressed.

Chapter 2

Theory of Momentum-Resolved Electron Energy Loss Spectroscopy

2.1 M-EELS Cross Section

It has long been known that inelastic scattering measurements give us valuable insights into the different Fourier-Transformed (FT-ed) correlation functions in many-particle systems [28]. For instance, the cross section for magnetic inelastic neutron scattering (INS) is proportional to the FT of the spin-spin correlation function, while the cross-section for inelastic X-ray scattering IXS is proportional to the FT of the electron density-electron density correlation function. For these measurements, one sends in a particle of well-defined energy, E_i, and momentum, $\mathbf{k}_i$, which scatters from excitations in the solid of interest and leaves with outgoing energy, E_f, and momentum, $\mathbf{k}_f$. Using the conservation laws of energy and momentum, one can deduce information about the collective excitations of the solid in question.

Momentum-resolved electron energy loss spectroscopy (M-EELS) is an inelastic scattering technique that uses low energy (typically 2-200eV) electrons to scatter from the surface of a solid. The relationship between the scattering cross section and the appropriate response function is presented here to give a quantitative understanding of the relevant response and correlation functions measured with this technique. To determine the cross section, one uses the formalism of Fermi's Golden Rule, which can be derived from quantum mechanical time-dependent perturbation theory [29]. This leads one to examine the following matrix element:

$$M = -\frac{i}{\hbar} \langle f | H'(0) | i \rangle \tag{2.1}$$

where $|i\rangle$ and $|f\rangle$ denote the initial and final states of the entire system comprising the scattering electron and the sample. For the case of M-EELS, the relevant interaction is the instantaneous Coulomb interaction,

$$H' = \frac{e^2}{2} \int \frac{\hat{\rho}(\mathbf{R}_1)\hat{\rho}(\mathbf{R}_2)}{|\mathbf{R}_1 - \mathbf{R}_2|} \tag{2.2}$$

where $\hat{\rho}$ is the electron number density operator and the coordinate $\mathbf{R} = (\mathbf{r}, z)$, where $\mathbf{r}$ and z are components parallel and perpendicular to the surface, respectively. In terms of this interaction, the scattering matrix element is given by

$$M = \frac{e^2}{2} \int \frac{\langle n | \hat{\rho}(\mathbf{R}_1) | m \rangle \psi_s^*(\mathbf{R}_2)\psi_i(\mathbf{R}_2)}{|\mathbf{R}_1 - \mathbf{R}_2|} \tag{2.3}$$

where ψ_i and ψ_s are the wave functions for the initial and final state of the probe electron, and $|m\rangle$ denotes a many-body eigenstate of the semi-infinite material system. Following past practice in the M-EELS field, in Eq. 2.3 we have neglected exchange scattering, which can be important if the overlap between the probe and valence electron wave functions is significant [30–32]. In so doing we have neglected the possibility of spin-dependent scattering, which can be significant in materials exhibiting pronounced magnetic excitations, such as magnons.

In M-EELS, multiple scattering effects are significant. One of the crucial milestones for the technique was the recognition that multiple scattering predominantly takes place in the elastic, rather than the inelastic, channel. This suggests that the scattering can be accurately described by using wave functions for the probe electron that are modified from their nominally plane-wave form, and treating the inelastic scattering in the Born approximation. As was argued earlier by Mills, the appropriate incident and scattered

wave functions, ψ_i and ψ_s, are [31]:

$$\begin{aligned} \psi_i(\mathbf{R}) &= N_i \left(e^{i\mathbf{k}_i\cdot\mathbf{r}} e^{ik_i^z z} + R_i e^{i\mathbf{k}_i\cdot\mathbf{r}} e^{-ik_i^z z} \right) \theta(z) \\ \psi_s(\mathbf{R}) &= N_s \left(e^{i\mathbf{k}_s\cdot\mathbf{r}} e^{ik_s^z z} + R_s e^{i\mathbf{k}_s\cdot\mathbf{r}} e^{-ik_s^z z} \right) \theta(z). \end{aligned} \tag{2.4}$$

In this expression, R_i and R_s describe the effect of specular reflection of the incident or scattered plane wave off the sample surface, and the step function, $\theta(z)$, implies that the wave functions do not penetrate into the material, which we take to fill the half-space $z < 0$. N_i and N_s are normalization constants that, if the phase shift due to the reflection is small, have the form [30,31]:

$$N_{i,s} = \sqrt{\frac{2}{V\left(1 + |R_{i,s}|^2\right)}}. \tag{2.5}$$

Inserting these expressions into Eq. 2.3 results in four distinct terms that contribute to the inelastic scattering cross section. As was shown previously by Mills, the matrix element is dominated by the cross terms, which involve single powers of R_i and R_s. Keeping only these two terms, the matrix element is given by [31]:

$$M = M_i + M_s \tag{2.6}$$

where

$$M_{i,s} = -\frac{ie^2}{2\hbar} N R_{i,s} \int \frac{\langle n|\, \hat{\rho}(\mathbf{R}_1)\, |m\rangle\, e^{i\mathbf{q}\cdot\mathbf{r}_2} e^{\mp i\left(k_s^z + k_i^z\right) z_2} \theta(z_2)}{|\mathbf{R}_1 - \mathbf{R}_2|} d\mathbf{R}_1 d\mathbf{R}_2 \tag{2.7}$$

where $N = \sqrt{N_i N_s}$ and $\mathbf{q}$ is the in-plane component of the momentum transfer. A schematic of the relevant processes are shown in Fig. 2.1.

Expressed explicitly in terms of in- and out-of-plane coordinates,

$$M_{i,s} = -\frac{ie^2}{2\hbar} N^2 R_{i,s} \int \frac{\langle n|\, \hat{\rho}(\mathbf{r}_1, z_1)\, |m\rangle\, e^{i\mathbf{q}\cdot\mathbf{r}_2} e^{\mp i\left(k_s^z + k_i^z\right) z_2} \theta(z_2)}{\sqrt{(r_1 - r_2)^2 + (z_1 - z_2)^2}} d\mathbf{r}_1^2 d\mathbf{r}_2^2 dz_1 dz_2. \tag{2.8}$$

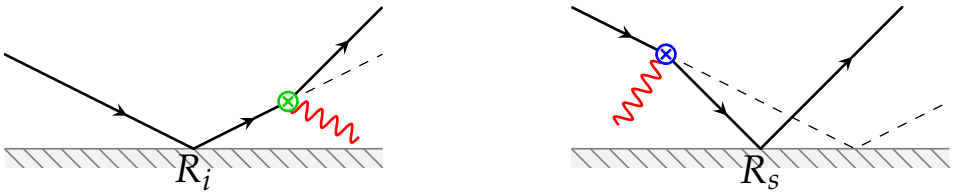

Figure 2.1: Schematic of relevant matrix elements in the scattering cross section

We begin by considering M_s only. Performing the r_2 integral yields

$$M_s = -\frac{i}{2\hbar} N^2 R_s \, V_{2D}(q) \int d\mathbf{r}_1^2 dz_1 dz_2 \, \langle n | \, \hat{\rho}(\mathbf{r}_1, z_1) \, | m \rangle \, e^{i\left(k_s^z + k_i^z\right) z_2} \theta(z_2) \, e^{i\mathbf{q}\cdot\mathbf{r}_1} \, e^{-q|z_1 - z_2|} \tag{2.9}$$

where $q = |\mathbf{q}|$ and $V_{2D}(q) = 2\pi e^2/q$ is the FT of the Coulomb interaction in two dimensions. The $\mathbf{r}_1$ integral is a Fourier transform, so

$$M_s = -\frac{i}{2\hbar} N^2 R_s \, V_{2D}(q) \int_{-\infty}^{0} dz_1 \, \langle n | \, \hat{\rho}\left(\mathbf{q}, z_1\right) | m \rangle \int_0^{\infty} dz_2 e^{i\left(k_s^z + k_i^z\right) z_2} e^{-q|z_1 - z_2|}, \tag{2.10}$$

where we have used the fact that the material is semi-infinite, i.e., the z_1 integrand is non-zero only for $z_1 < 0$. The quantity $(z_1 - z_2)$ is always negative, so the z_2 integral may readily be done to yield

$$M_s = \frac{N^2 R_s}{2\hbar} \frac{V_{2D}(q)}{k_s^z + k_i^z + iq} \int_{-\infty}^{0} \langle n | \, \hat{\rho}\left(\mathbf{q}, z_1\right) | m \rangle \, e^{q z_1}. \tag{2.11}$$

In this form, it is clear why the cross terms, Eq. 2.6, dominate the scattering cross section. In high energy, bulk-sensitive EELS, the inelastic cross section $\sim 1/q^4$, i.e., is a rapidly decreasing function of q. In cross terms like Eq. 2.11, however, the denominator contains the sum $k_s^z + k_i^z$, rather than the difference $q^z = k_s^z - k_i^z$, q^z being the out-of-plane component of the momentum transfer. Hence, in the so-called "dipole" regime, in which measurements are carried out in near-specular geometry, $k_s^z \approx -k_i^z$, so the sum approximately vanishes and only the in-plane component, q, appears in the denominator.

The overall effect is that the probe electron undergoes a large change in its out-of-plane momentum, but this transferred momentum comes "for free," in the sense that it does not enter the effective FT-ed Coulomb interaction, the momentum being supplied by the reflectance from the sample surface, rather than the inelastic event.

The other part of the matrix element, M_i, is identical to the above, with $R_s \to R_i$ and $k_s^z + k_i^z \to -k_s^z - k_i^z$. This gives

$$M_i = \frac{N^2 R_i}{2\hbar} \frac{V_{2D}(q)}{-k_s^z - k_i^z + iq} \int_{-\infty}^{0} dz_1 \, \langle n| \, \hat{\rho}\left(\mathbf{q}, z_1\right) |m\rangle \, e^{qz_1}. \tag{2.12}$$

The full matrix element $M = M_i + M_s$ is then

$$M = \frac{-i}{\hbar} N^2 R \frac{4\pi e^2}{\left(k_s^z + k_i^z\right)^2 + q^2} \int_{-\infty}^{0} dz_1 \, \langle n| \, \hat{\rho}\left(\mathbf{q}, z_1\right) |m\rangle \, e^{qz_1} \tag{2.13}$$

where for simplicity we have assumed $R_s = R_i = R$.

To turn this matrix element into a scattering cross section we take the traditional route of applying Fermi's Golden Rule. The double differential scattering cross section is defined as

$$\frac{\partial^2 \sigma}{\partial \Omega \partial E} = \frac{1}{\Phi} \sum_f w_{i \to f} \cdot \frac{\partial^2 N}{\partial \Omega \partial E} \tag{2.14}$$

where Φ is the incident flux and $\partial^2 N / \partial \Omega \partial E$ is the density of final states of the scattered electron. The matrix element enters in the transition rate

$$w_{i \to f} = \frac{2\pi}{\hbar} \left| \langle f| \, H'(0) \, |i\rangle \right|^2 = 2\pi\hbar \, |M|^2. \tag{2.15}$$

For a single, non-relativistic electron travelling at velocity v, $\Phi = v/V = \sqrt{2E_i/m}/V$, where E_i is the incident electron kinetic energy and V is the volume of all space. The density of final states is given by the usual expression

$$\frac{\partial^2 N}{\partial\Omega\partial E} = \frac{V}{8\pi^3}\left(\frac{2m}{\hbar^2}\right)^{3/2}\sqrt{E}. \tag{2.16}$$

Squaring the matrix element, the final result is

$$\frac{\partial^2\sigma}{\partial\Omega\partial E} = \sigma_0\left[V_{eff}(k_i^z, k_s^z, q)\right]^2 \int_{-\infty}^{0} dz_1 dz_2 e^{q(z_1+z_2)} \sum_{m,n} \langle n|\,\hat{\rho}\,(\mathbf{q}, z_1)\,|m\rangle\,\langle m|\,\hat{\rho}\,(-\mathbf{q}, z_2)\,|n\rangle$$
$$\times\, P_m \delta\,(E - E_n + E_m) \tag{2.17}$$

where

$$\sigma_0 \equiv \sqrt{\frac{E_f}{E_i}}\frac{m^2}{2\pi^2\hbar^4}\frac{|R|^2}{\left(1+|R|^2\right)^2} \tag{2.18}$$

and

$$V_{eff}(k_i^z, k_s^z, q) \equiv \frac{4\pi e^2}{\left(k_s^z + k_i^z\right)^2 + q^2} \tag{2.19}$$

is an effective FT-ed Coulomb interaction that describes how the probe electron couples to excitations near the surface of a semi-infinite system. From this result we can already confirm the crucial observation, made previously by Mills, that the probe depth in M-EELS is not set by the penetration depth of the electrons, as it is in other electron spectroscopies such as angle-resolved photoemission (ARPES) or scanning tunneling microscopy (STM), but by the inverse of the in-plane component of the momentum transfer, q [31]. The reason is that M-EELS measures the dielectric response of the surface, which is coupled electromagnetically to layers deeper in the material. Hence, at low q, the technique can couple to features deep in the sample, via their influence on the dielectric response near the surface.

2.2 Fluctuation-Dissipation Theorem for HR-EELS

We are now ready to establish a relationship between the cross section, Eq. 2.17, a correlation function for the density, and a density response function. In complete generality, for a many-body system, the density correlation function is defined as [33]:

$$S(\mathbf{R}_1, \mathbf{R}_2, \omega) = \frac{1}{\hbar} \sum_{m,n} \langle m| \hat{\rho}(\mathbf{R}_1) |n\rangle \langle n| \hat{\rho}(\mathbf{R}_2) |m\rangle P_m \delta(\omega - \omega_n + \omega_m) \tag{2.20}$$

in real space. This quantity can also be expressed in momentum space,

$$S(\mathbf{Q}_1, \mathbf{Q}_2, \omega) = \frac{1}{\hbar} \sum_{m,n} \langle m| \hat{\rho}(\mathbf{Q}_1) |n\rangle \langle n| \hat{\rho}(-\mathbf{Q}_2) |m\rangle P_m \delta(\omega - \omega_n + \omega_m) \tag{2.21}$$

where we have adopted the momentum notation $\mathbf{Q} = (\mathbf{q}, q_z)$, where $\mathbf{q}$ and q_z are the in-plane and out-of-plane components, respectively. For relation to the cross section, we consider here the mixed representation,

$$S(\mathbf{q}_1, z_1; \mathbf{q}_2, z_2; \omega) = \frac{1}{\hbar} \sum_{m,n} \langle m| \hat{\rho}(\mathbf{q}_1, z_1) |n\rangle \langle n| \hat{\rho}(-\mathbf{q}_2, z_2) |m\rangle P_m \delta(\omega - \omega_n + \omega_m). \tag{2.22}$$

In terms of this quantity, Eq. 2.17 may be written,

$$\frac{\partial^2 \sigma}{\partial \Omega \partial E} = \sigma_0 \left[V_{eff}(k_i^z, k_s^z, q) \right]^2 \int_{-\infty}^{0} dz_1 dz_2 e^{q(z_1+z_2)} S(\mathbf{q}, z_1; \mathbf{q}, z_2; \omega) \tag{2.23}$$

This confirms the notion that, M-EELS directly measures a correlation function for the charge density in the region near the surface of the material [30]. To complete our study, we must identify a relationship between this quantity and a causal response function.

The the density response function is defined as [33]:

$$\chi(\mathbf{R}_1, \mathbf{R}_2; t_1 - t_2) = -\frac{i}{\hbar} \sum_m P_m \langle m| \left[\hat{\rho}(\mathbf{R}_1, t_1), \hat{\rho}(\mathbf{R}_2, t_2)\right] |m\rangle \; \theta(t_1 - t_2) \tag{2.24}$$

where $[,]$ represents a commutator. In contrast to the correlation function, $\chi(\mathbf{R}_1, \mathbf{R}_2; t_1 - t_2)$ is a propagator for the charge density, i.e., it represents the amplitude that a disturbance in the density at location $\mathbf{R}_2$ will propagate to $\mathbf{R}_1$ after elapsed time $t_1 - t_2$. In contrast to S, χ is a microscopic representation of the collective charge dynamics of the system, exhibiting causality enforced by the $\theta(t_1 - t_2)$ term, which mandates that disturbances in the density can only influence the state of the system at later times. Written out explicitly in the mixed representation, the response function has the form

$$\chi(\mathbf{q}_1, z_1; \mathbf{q}_2, z_2, \omega) = \frac{1}{\hbar} \left[\frac{\langle m| \hat{\rho}(\mathbf{q}_1, z_1) |n\rangle \langle n| \hat{\rho}(\mathbf{q}_2, z_2) |m\rangle}{\omega - \omega_n + \omega_m + i\eta} - \frac{\langle m| \hat{\rho}(\mathbf{q}_1, z_1) |n\rangle \langle n| \hat{\rho}(\mathbf{q}_2, z_2) |m\rangle}{\omega + \omega_n - \omega_m + i\eta} \right]. \tag{2.25}$$

To relate this quantity to the correlation function, we begin by taking its imaginary part. Using the relation

$$\mathrm{Im}\left[\frac{1}{x + i\eta}\right] = -\pi \, \delta(x) \tag{2.26}$$

for infinitesimal η we get

$$\begin{aligned} \mathrm{Im}\left[\chi(\mathbf{q}, z_1; -\mathbf{q}, z_2, \omega)\right] = -\frac{\pi}{\hbar} \sum_{m,n} P_m \big[&\langle m| \hat{\rho}(\mathbf{q}, z_1) |n\rangle \langle n| \hat{\rho}(-\mathbf{q}, z_2) |m\rangle \; \delta(\omega - \omega_n + \omega_m) \\ - &\langle m| \hat{\rho}(\mathbf{q}, z_1) |n\rangle \langle n| \hat{\rho}(-\mathbf{q}, z_2) |m\rangle \, \delta(\omega + \omega_n - \omega_m) \big] \end{aligned} \tag{2.27}$$

where, anticipating a comparison to Eq. 2.22, we have chosen the specific case $\mathbf{q}_1 =$

$-\mathbf{q}_2 = \mathbf{q}$. The first term is identical to the correlation function,

$$\begin{aligned}\mathrm{Im}\left[\chi(\mathbf{q}, z_1; -\mathbf{q}, z_2, \omega)\right] &= -\pi S(\mathbf{q}, z_1; \mathbf{q}, z_2; \omega) \\ &+ \frac{\pi}{\hbar}\sum_{m,n} P_m \left[\langle m|\,\hat{\rho}(\mathbf{q}, z_1)\,|n\rangle\,\langle n|\,\hat{\rho}(-\mathbf{q}, z_2)\,|m\rangle\,\delta\left(\omega + \omega_n - \omega_m\right)\right].\end{aligned} \tag{2.28}$$

To deal with the second term, we recognize that

$$P_n = P_m e^{-\beta(E_n - E_m)} = P_m e^{-\beta\hbar\omega}. \tag{2.29}$$

Substituting this into Eq. 2.28 and exchanging the indices m and n gives

$$\mathrm{Im}\left[\chi(\mathbf{q}, z_1; -\mathbf{q}, z_2, \omega)\right] = -\pi S(\mathbf{q}, z_1; \mathbf{q}, z_2; \omega) + \pi e^{\beta\hbar\omega} S(-\mathbf{q}, z_1; -\mathbf{q}, z_2; \omega) \tag{2.30}$$

or, equivalently,

$$S(\mathbf{q}, z_1; \mathbf{q}, z_2; \omega) = -\frac{1}{\pi}\frac{1}{1 - e^{\beta\hbar\omega}}\mathrm{Im}\left[\chi(\mathbf{q}, z_1; -\mathbf{q}, z_2, \omega)\right]. \tag{2.31}$$

Eq. 2.31 is a statement of the fluctuation-dissipation theorem relevant to momentum-resolved electron energy loss spectroscopy. Its physical meaning is that the scattered intensity, which is directly proportional to the correlation function, S, is also a measure of the dissipative, imaginary part of the propagator that describes the charge dynamics. The proportionality factor, $n(\omega) = (1 - \exp\beta\hbar\omega)^{-1}$, is the so-called Bose factor, which mandates that the excitations that contribute to S exhibit Bose statistics, which is required for a two-particle response function.

2.3 Relationship to the Inverse Dielectric Function

It is known that for a three dimensional translationally invariant system that the imaginary part of the longitudinal inverse dielectric function, also known as the loss function or energy loss function, is related to the charge density response function, $\chi(\mathbf{q},\omega)$, as so [33]:

$$\mathrm{Im}\left(\frac{1}{\epsilon^L(\mathbf{q},\omega)}\right) = V(\mathbf{q})\,\mathrm{Im}(\chi(\mathbf{q},\omega)), \tag{2.32}$$

where

$$V(\mathbf{q}) = \frac{4\pi e^2}{\mathbf{q}^2}. \tag{2.33}$$

However, as can be seen from Eq. 2.23 and Eq. 2.31, M-EELS does not probe the three dimensional response function, but instead a surface response function.

In most of this thesis, quasi-2D layered materials are studied that are van der Waals bonded along the c-axis. Under the assumption that the in-plane surface response and the in-plane bulk response are not drastically different, it may be possible to establish a relationship between the in-plane surface response function and the in-plane bulk dielectric function. Mills has previously noted that the M-EELS cross section for a three-dimensional solid is related to the inverse dielectric function at small in-plane momentum transfers as so [34]:

$$\frac{\partial^2\sigma}{\partial\Omega\partial E} \propto \mathrm{Im}\,\frac{-1}{\epsilon+1} \tag{2.34}$$

This relationship has been shown to work well in a seminal EELS paper by Ibach on ZnO [35]. It is not known, though, whether the relationship in Eq. 2.34, or a modified relationship between the bulk and surface in-plane response, is needed for quasi-2D layered materials. This relationship will depend on the penetration depth (compared to the c-axis lattice parameter) of the probe electron, which will in turn be material-dependent.

Therefore, the relationship between the in-plane surface charge density response function will be tested on a case-by-case basis by comparing to in-plane optical data at $\mathbf{q}=0$, where the spectra are expected to be similar for non-superconducting compounds in the limit that the surface and bulk in-plane responses are the same.

Chapter 3

Instrumentation

3.1 Chamber Design

To accommodate the instruments used in the experiments, it was necessary to house the spectrometers in ultra-high vacuum (UHV) chambers. This was necessary for two main reasons: (1) since the probe is surface-sensitive, contamination by adsorbates hinders access of the probe electrons to the sample surface and (2) the filament used to emit electrons only works under UHV conditions (to prevent oxidation of the heated filament).

Therefore, the design of two vacuum chambers, one to house the M-EELS spectrometer, and one to house the low-energy electron diffraction (LEED) instrumentation was undertaken. Both chambers had design targets that needed to be met. For the M-EELS chamber, it was necessary to achieve a vacuum level of $<5\times10^{-10}$ Torr, a stray magnetic field level of $<$15 mG, a cryostat temperature of $<$20 K. Furthermore, it was necessary that we had the capability to put the sample in the center of rotation (COR) of its rotation axis and the ability to align this sample rotation axis with the COR of the spectrometer. For the LEED chamber, it was necessary to achieve a vacuum level of $<5\times10^{-10}$ Torr, to be able to transfer in samples, to cleave samples, and also to align samples to ensure quick determination of surface quality through LEED spectra.

The vacuum target for the M-EELS chamber was ensured by equipping it with a 400L/s turbomolecular pump backed by a scroll pump, an ion pump and a low temperature titanium sublimation pump. In addition, the vacuum chamber was baked out periodically to rid the chamber of adsorbates that outgas (such as water vapor). The pres-

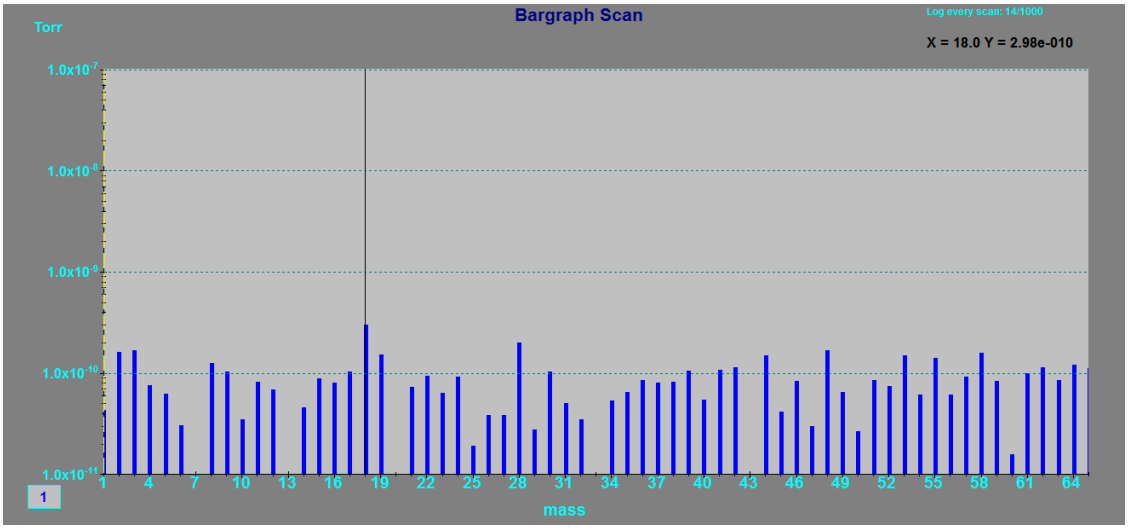

Figure 3.1: Typical Residual Gas Analyzer Spectrum under UHV Conditions

sure was measured using a Granville-Phillips Stabil-Ion gauge, which enables measurements down to $\sim 10^{-12}$ Torr. Because the ion gauge is calibrated to measure the pressure of nitrogen (N_2) gas, a residual gas analyzer (RGA) comprising a quadrupole mass spectrometer was used to measure the partial pressures in the chamber. A typical spectrum from the RGA is shown in Fig. 3.1, which comprises mostly noise. The vacuum target of the LEED chamber was met by reducing the volume of the chamber markedly compared to the M-EELS chamber, and using only the turbomolecular pump backed by the scroll pump for evacuation. Bakeout was also periodically undertaken for this chamber to reduce outgassing rates.

The chambers were connected to each other and to the load lock (where the samples are loaded into the chamber) through a series of gate valves. These gate valves can maintain an ultra-high vacuum on one side and atmospheric pressure on the other. The load lock is pumped down using a turbomolecular pump backed by a diaphragm pump and can reach a vacuum of $\sim 10^{-7}$ Torr.

The magnetic field specification was necessary in order to reduce the amount of stray field in the M-EELS chamber. The main problem associated with stray fields lie in their ability to deflect low-energy electrons. The main source of stray fields is the earth's mag-

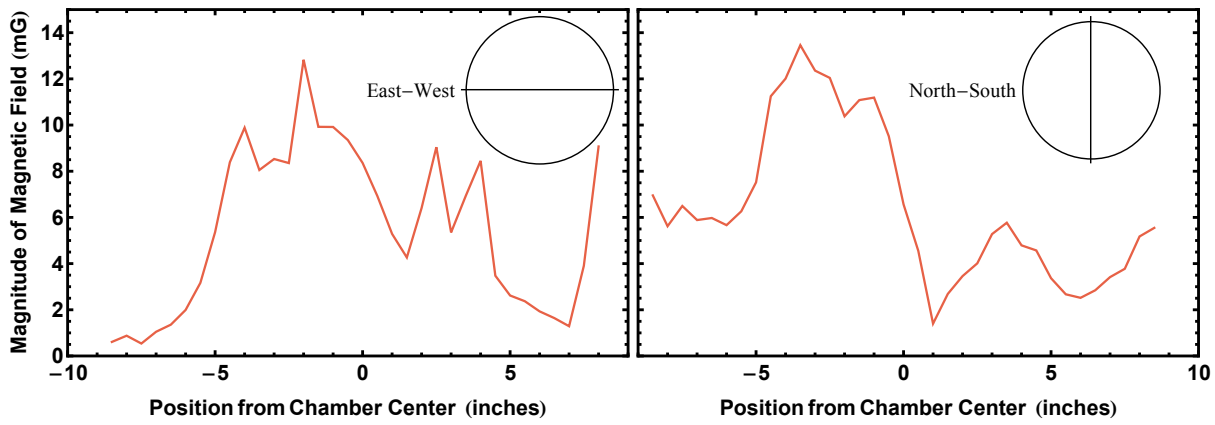

Figure 3.2: Stray Magnetic Field Mapping

netic field, which has a magnitude of ∼450 mG. Therefore, two layers of μ-metal, each approximately 2 mm thick, were fashioned to line the inside walls of the M-EELS chamber. A μ-metal layer of ∼1 mm was also used to line the LEED instrumentation. To ensure that the magnetic field in the M-EELS chamber met the target specifications, we measured the three components of the stray field inside the chamber using a Hall probe in three different orientations. The stray field components were also measured along two lines, east-west and north-south, in half-inch increments across the inside of the M-EELS vacuum chamber. The results are summarized in Fig. 3.2 after vectorially adding the individual components.

The temperature specification of the chamber was met by designing a sample holder that attached to the end of a Janis ST-400 UHV cold finger cryostat which is cooled by conduction using liquid helium external to the chamber. Because the sample holder was mounted on a thermally insulating rotation stage, a copper braid was e-beam welded to a centering ring. This was required for appropriate thermal contact and conduction. A radiation shield was used to protect the sample from radiation heating, which is the main source of loss of cooling power. An image of this assembly is shown in Fig. 3.3.

The temperature at the sample position was calibrated using a silicon temperature diode. The results of the calibration are shown in Fig. 3.4, demonstrating that the tem-

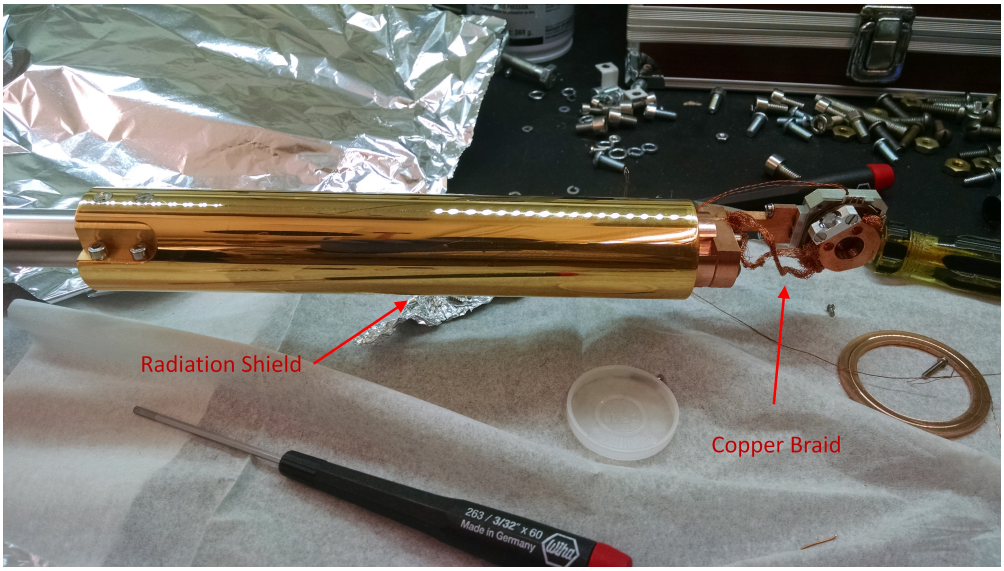

Figure 3.3: Image of Sample Holder Assembly

perature of the sample reaches ∼17 K at the base temperature of the cryostat. In a typical experiment, an hour is needed for the sample temperature to equilibrate.

3.2 Sample Holder Design

Both the M-EELS and LEED chambers were equipped with a sample holder to house sample pucks on which samples were mounted. A drawing of the sample puck design is shown in Fig. 3.5. Samples attached to the sample pucks were transported into and out of the chambers during sample transfer. They were designed to fit in the magnetically-coupled transfer manipulators as shown in Fig. 3.6.

The sample holder in the LEED chamber was designed so that two pucks could be held at a given time. An image of the LEED sample holder can be seen in Fig. 3.7.
This sample holder was also equipped with a button heater (capable of reaching ∼800 C), so that sample surfaces could be prepared by annealing when this was an option. The sample holder was attached to rod that was externally translatable using a gimbal and z-stage to allow for an x-, y- and z-translation to ensure successful transfer and also to

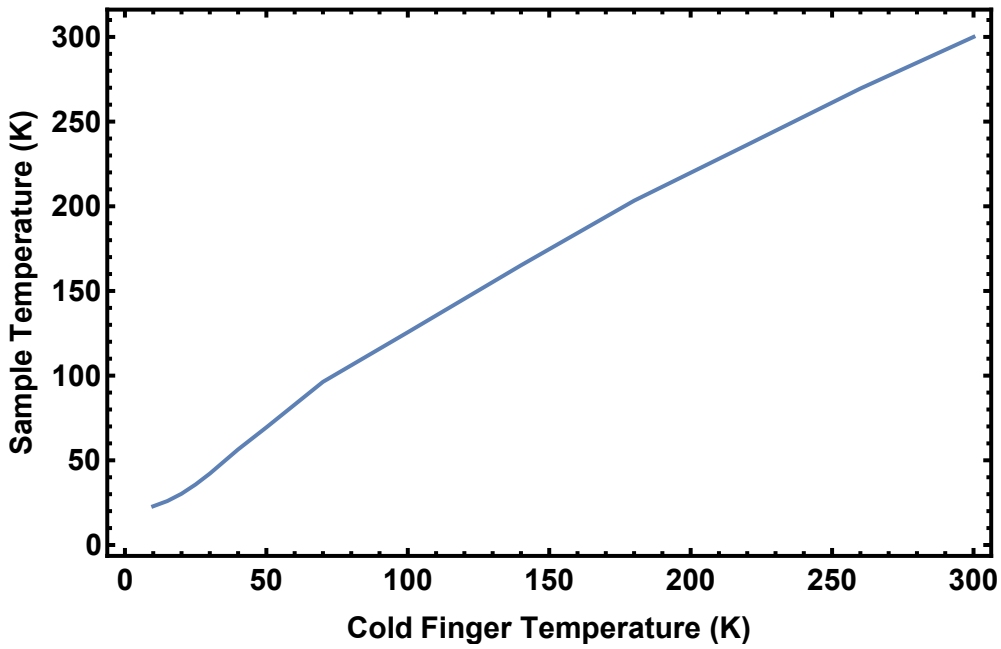

Figure 3.4: Temperature Calibration Curve

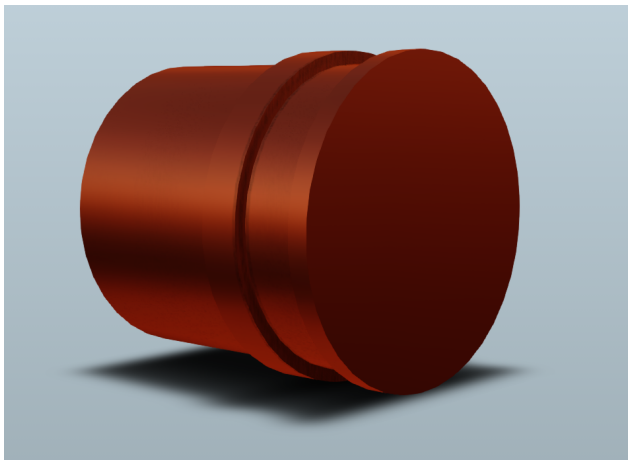

Figure 3.5: Rendering of Sample Puck

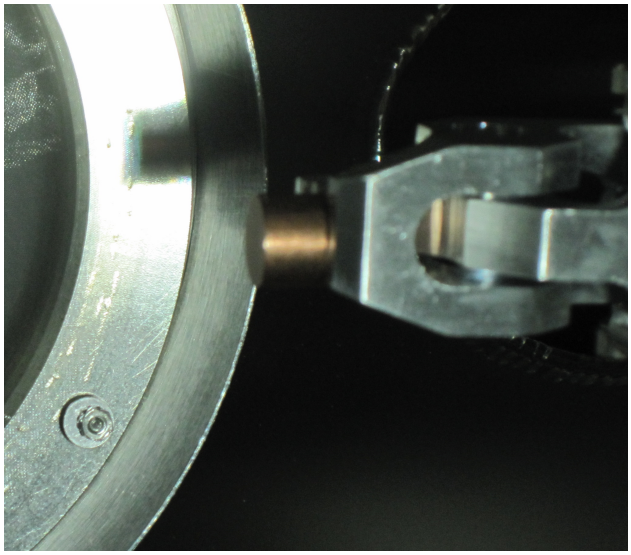

Figure 3.6: Image of Sample Transfer Mechanism

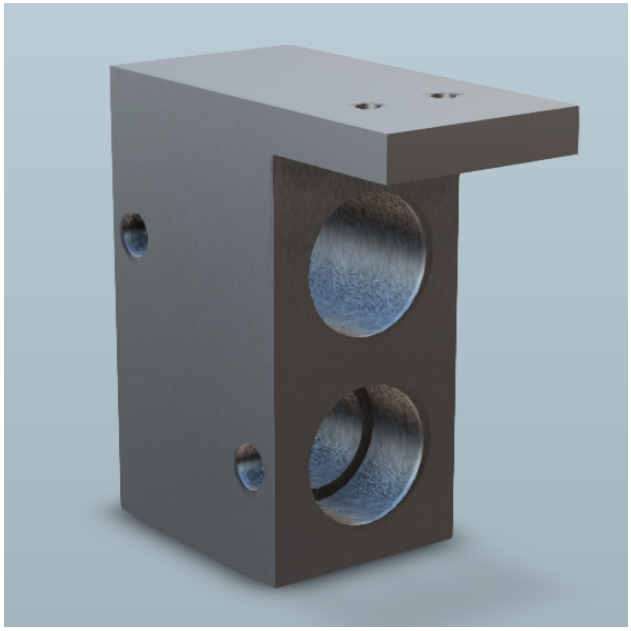

Figure 3.7: Rendering of Sample Holder in LEED Chamber

ensure precise positioning to obtain a LEED pattern. The pucks were held in the slots using spring plungers which were held in place using lock washers.

The sample holder in the M-EELS chamber is pictured in Fig. 3.3 and Fig. 3.8. This sample holder, was also capable of x-, y- and z- motion to allow for sample transfer. In contrast to the LEED sample holder, where spring plungers were used to keep the sample fixed, a set screw was used. The set screw was tightened in-situ using a UHV compatible wobble stick. An image of the sample holder with a puck loaded and sample attached is given in Fig. 3.8. The set screw can be seen on the left side of this image.

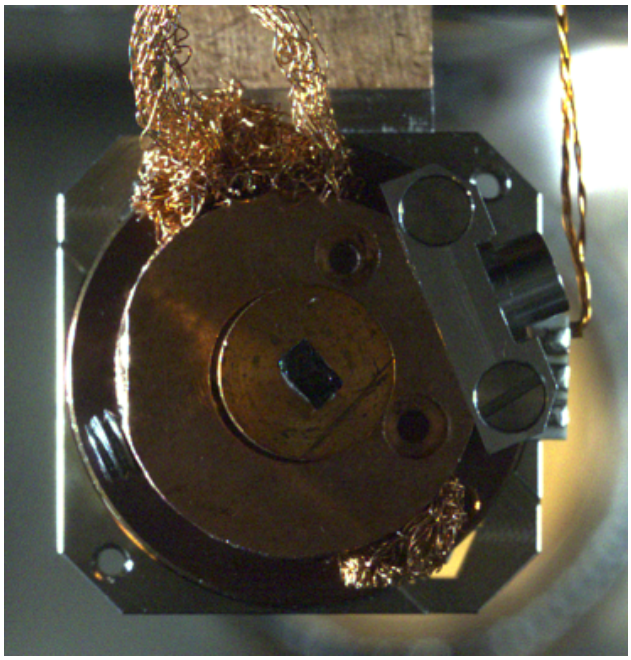

Figure 3.8: Image of M-EELS Sample Holder with Sample Loaded

3.3 Sample Preparation and Sample Transfer

The sample preparation and transfer procedure is best communicated in recipe form:

1. Cut the single crystal to an appopriate size to fit on the sample holder.

2. Use a silver epoxy (EPO-TEK H20E) to mount the sample to the puck and heat to 120^oC for about two-three hours.

3. With sample attached to the puck, orient sample with Laue instrument and use a diamond-tipped pen to mark desired orientation. A typical Laue pattern is shown in Fig. 3.9.

4. Use Torr Seal to attach an aluminum post to the sample surface and 120^oC for about 20-30 minutes.

5. Load the oriented sample into the load lock attached to the LEED chamber by inserting the puck into the magnetic manipulator.

6. Pump down the load lock and wait *at least* 45 min till the pressure reaches 8×10^{-7} Torr.

7. Open the gate valve to the LEED chamber and load the sample into one of the slots on the sample holder.

8. Retract the magnetic manipulator back into the load lock and close the gate valve to the load lock. Wait until the pressure in the LEED chamber recovers to at least 7×10^{-10} Torr.

9. Prepare the sample surface by either heating the sample or by cleaving the sample.

10. Check the surface quality by obtaining a LEED pattern. A typical LEED pattern for muscovite is shown in Fig. 3.10.

11. Open the gate valve to the M-EELS chamber and pull out the sample puck using the magnetic manipulator from the M-EELS chamber.

12. Load the puck into the M-EELS sample holder, and while still holding the puck with the magnetic manipulator, tighten the set screw to keep the sample in place.

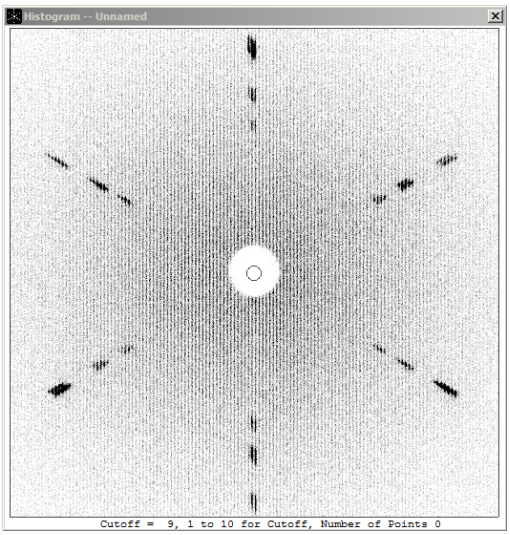

Figure 3.9: Laue Image of $TiSe_2$

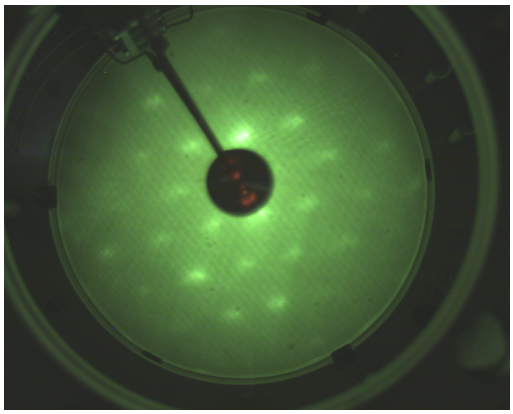

Figure 3.10: LEED Image of Muscovite

13. Before starting an experiment, align the beam with appropriate voltages as specified in the manual.

3.4 Center of Rotation

Putting the sample in the center of rotation of the M-EELS spectrometer was the main instrumentation-based innovation in this thesis. Prior to using the method described below, M-EELS experiments would be conducted by rotating only the detector arm, keeping the sample position fixed. It was assumed that because only the in-plane component of the momentum-transfer mattered, a rotation of the sample was not necessary. This assumption appears not to have been experimentally checked, however [30].

The steps that were necessary to establish that the sample was in the center of rotation was twofold: (1) confirm that the sample is in the center of rotation of its own rotation axis, denoted the θ axis, and (2) confirm that the rotation axis of the sample, θ, coincides with the center of rotation of the spectrometer, γ (this rotation axis is often called 2θ in the literature, but this nomenclature is avoided here as γ does not necessarily coincide with twice θ). The vertical assembly shown in Fig. 3.11 was constructed to make sure that

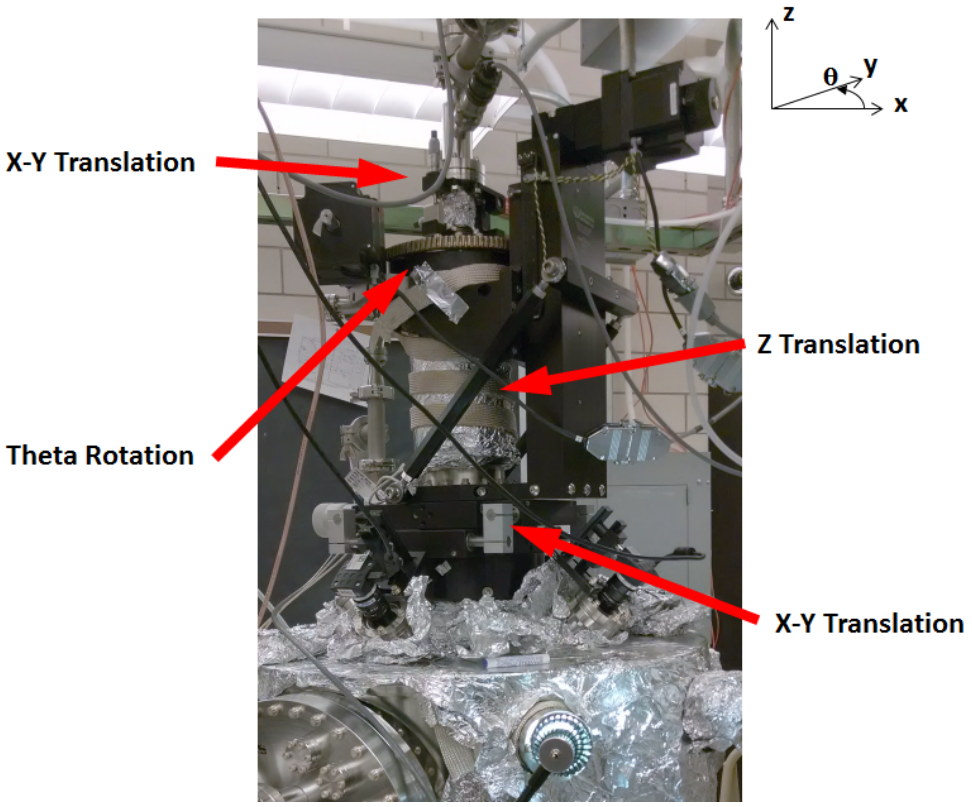

Figure 3.11: Image of the Center of Rotation Assembly

these steps could be adequately taken.

To ensure the sample was in the center of rotation of θ, a charge-coupled device (CCD) camera, equipped with a 25mm focal length lens, was mounted at a viewport external to the chamber to give a magnified view of the sample. Using the real-time camera viewing software, the sample surface was marked with cross-hairs with the sample face normal perpendicular to the camera viewing direction (see Fig. 3.12. The theta motor was rotated 180^o to see if the cross-hairs remained on the sample surface. If not, the center of rotation was found iteratively by moving the top X-Y micrometer positions. A typical view of the cross-hairs marking the center of rotation of θ from the camera can be seen in Fig. 3.12.

Once the sample was placed in the center of rotation of θ, placing the θ COR in the COR of γ was achieved by a trial-and-error method. First, the sample was positioned with the sample at half the detector angle (i.e. $\theta \approx 35^o$, γ=70^o). The bottom X-Y microm-

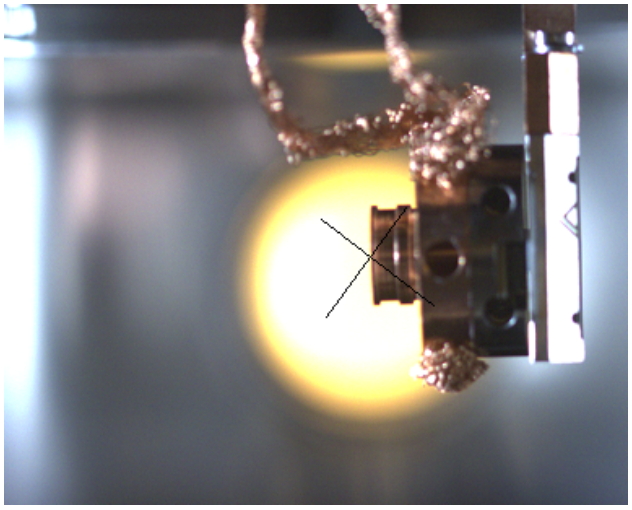

Figure 3.12: Image of the Sample Surface Marked with Cross-Hairs

eter positions were then adjusted to maximize the counts going into the detector. θ-scans ranging from -5 to +5 degrees from the starting value were then taken at a series of γ-θ values ($\theta \approx 35^o$, γ=70^o; $\theta \approx 32.5^o$, γ=65^o;...;$\theta \approx 20^o$, γ=10^o) to obtain the position of the specular reflection peak. A typical one of these θ scans showing a specular peak is plotted in Fig. 3.13.

Once this series of scans were obtained, the peaks in the θ-scans were fit with Gaussians and the peak position in θ was plotted against its corresponding γ value. These points were fit with a line and with a parabola. At the ideal position, the linear fit would give a slope of 1/2, while the parabolic correction would be as small as possible. Many positions were mapped out in effort to obtain these ideal values. A map of the positions attempted are shown in Fig. 3.14.

It was found that position 32 in Fig. 3.14 was optimal. A plot of the fits to the peak positions is presented in Fig. 3.15 (left). A plot of the fits to the peak positions at position 2 in the Fig. 3.15 (right) map is provided for reference.

The last important component in obtaining spectra throughout the Brillouin zone is the incoporation of a motor to rotate the sample along the axis perpendicular to the sample. This is usually dubbed the ϕ-rotation and is the terminology which will be used here.

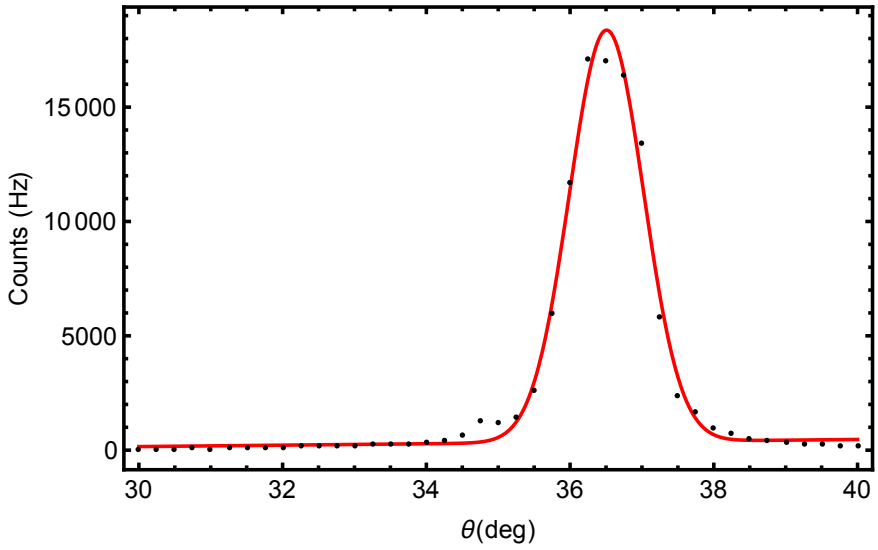

Figure 3.13: Plot of a Typical θ-Scan Showing a Specular Peak Fit with a Gaussian

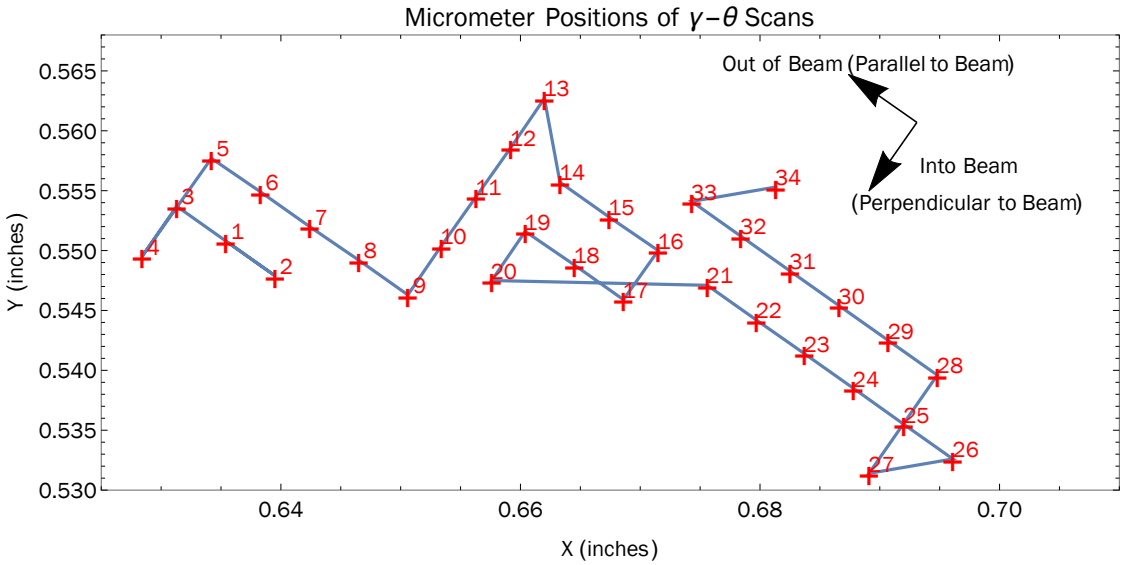

Figure 3.14: Map of the Bottom X-Y Stage Micrometer Positions

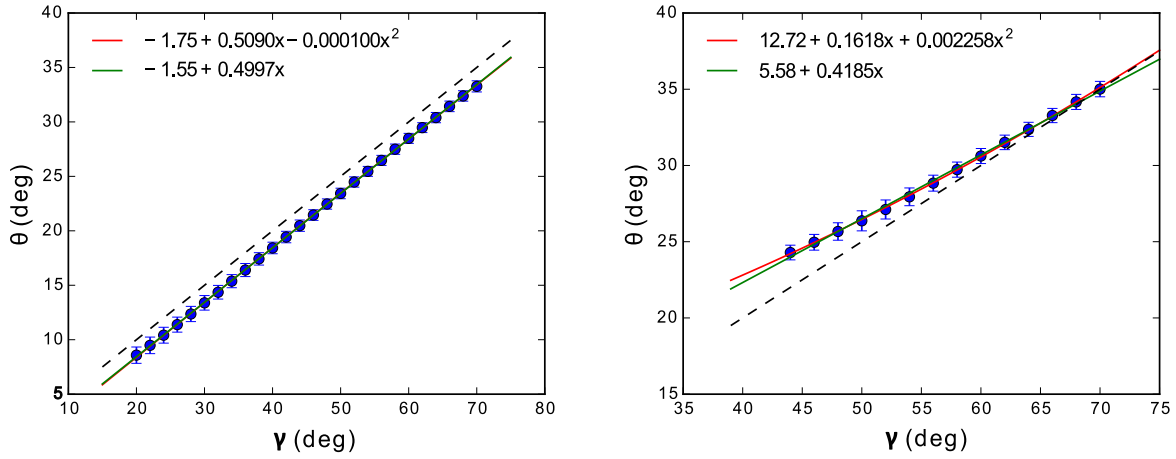

Figure 3.15: Fit to Peak Positions at Position 32 (left) and Position 2 (right) on the Map

The ϕ-rotation was accomplished through the use of a low-temperature UHV-compatible piezo-stepper motor stage which can be driven electrically, as opposed to mechanically. This allowed the electrical control of the motor through the use of electrical leads through the cryostat UHV feedthrough.

With all these components in place, we tested our COR alignment method by finding a Bragg peak. A thorough search through the literature suggests that the plots in Fig. 3.16 show the first observation of Bragg peaks using this kind of spectrometer with (H,K) denoting the surface Miller indices [30].

3.5 M-EELS Optics and Electronics

The M-EELS experiments were carried out with an Ibach-type electrostatic spectrometer [30]. The basic scheme of our experiment can be described as so:

1. A filament (here, LaB_6 is used) is heated that emits electrons.

2. The electron beam is passed through a cylindrical pre-monochromator and monochromator to select the incident beam energy with high energy resolution.

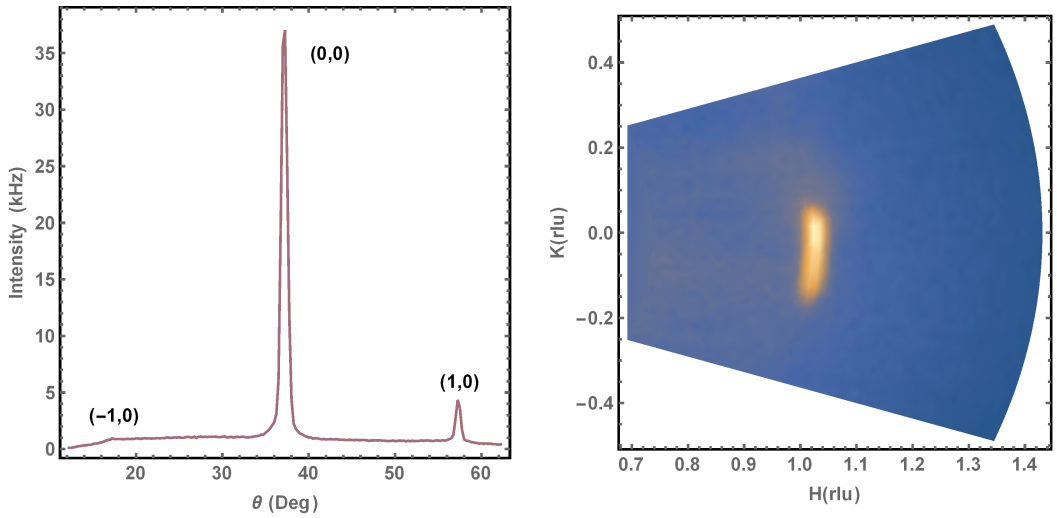

Figure 3.16: Observation of a (1,0) Bragg Peak in SmB_6 using an M-EELS Spectrometer

3. The electron beam interacts with the sample, which has been precisely placed in the COR.

4. The scattered beam is passed through the analyzer, which selects the energy of the outgoing beam.

5. The electrons exiting the analyzer hit an electron-multiplier where the electrical pulses generated can be read out through UHV feedthroughs.

6. The electrical pulses were fed through a pre-amplifier, an amplifier/disciminator, and coverted to a transistor-transistor logic (TTL) pulse and read by a National Instruments counter card.

7. The counts were read into SPEC, a software package usually used in conjunction with X-ray scattering experiments, to enable true reciprocal space mapping.

A schematic of the spectrometer is shown in Fig. 3.17. In a typical experiment, the current run through the LaB_6 filament was 1.75 Amps at approximately 3-3.1 Volts. This corresponds to a filament temperature of about 1850 K. The energy resolution, which also affected the momentum resolution, was adjusted by changing the potential differ-

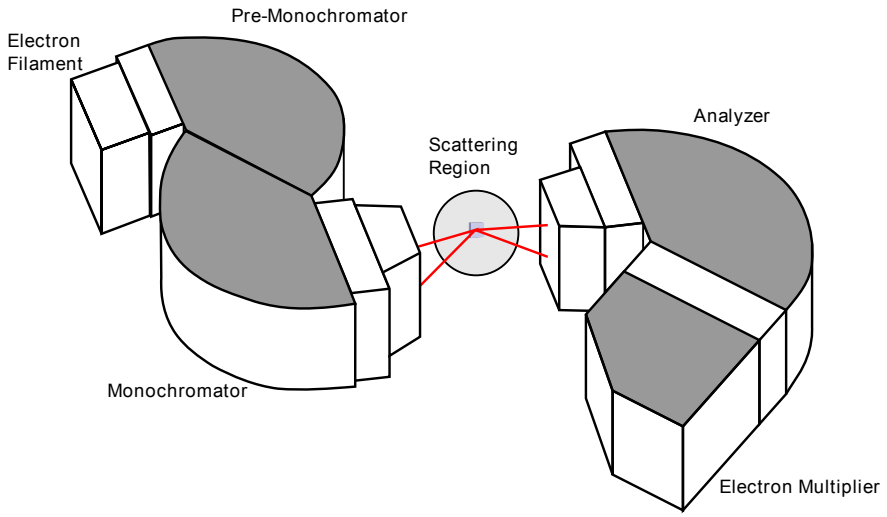

Figure 3.17: Schematic of the Optical Components Comprising the M-EELS System

ence between the inner and outer walls of the cylindrical deflectors on the monochromator and analyzer. The design details of the energy-dispersing cylindrical deflectors are thoroughly explained in Ref. [36]. Depending on beam energies and voltage settings of the electron-optical components, the energy and momentum resolution of the instrument ranged from 2 meV-5 meV and 0.02 Å^{-1} to 0.04 Å^{-1} respectively. Plots demonstrating typical energy and momentum scans with the corresponding resolution is shown in Fig. 3.18.

Lastly, it should be noted that the vertical beam divergence, set by the voltages on the electron-lenses that were located right before and after the scattering region, was estimated from the measurements of the Bragg peak in Fig. 3.16. The vertical beam divergence was determined to be approximately 10 degrees.

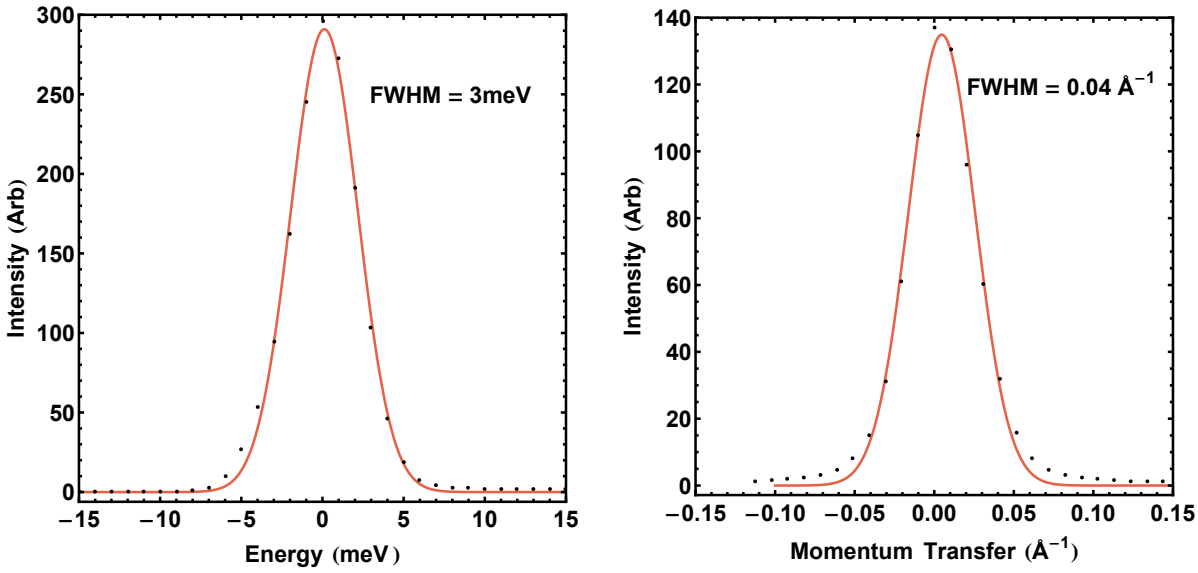

Figure 3.18: Energy and Momentum Resolution of a Typical M-EELS Experiment

Chapter 4

Collective Modes and Quasiparticle Dispersion Kinks

4.1 Kinks

With the rapid improvement in energy resolution of angle-resolved photoemission spectroscopy in the early part of this century, it became possible to map out the band structure of many families of materials with great accuracy [37]. One of the major discoveries, due to the improvement offered by increased energy resolution, was the presence of dispersion anomalies, usually denoted 'kinks' in the ARPES literature [13, 20, 38–41]. A schematic of a kink is shown in Fig. 4.1. The origin of these kinks in the literature is much debated, and are often speculated to occur from either band structure effects, such as avoided crossings, or from a coupling to a bosonic collective mode, such as phonons, magnons or more exotic collective excitations [13, 38–41]. It should be stressed that kinks originating from phonons are expected in normal metals and were predicted to exist well before their experimental observation with ARPES (see e.g. Ref [5] Chapt. 26). The framework outlined in Ref [5] is within a Hartree-Fock scheme where the change in the quasiparticle dispersion is expected to be of the form (at T=0):

$$\Delta E_{\mathbf{k}} = -\int_{\mathbf{k'}<\mathbf{k}_F} d\mathbf{k'} \frac{V(|\mathbf{k}-\mathbf{k'}|)}{\epsilon^L(\mathbf{k}\text{-}\mathbf{k'},\omega)}, \tag{4.1}$$

where

$$V(\mathbf{q}) = \frac{4\pi e^2}{\mathbf{q}^2} \tag{4.2}$$

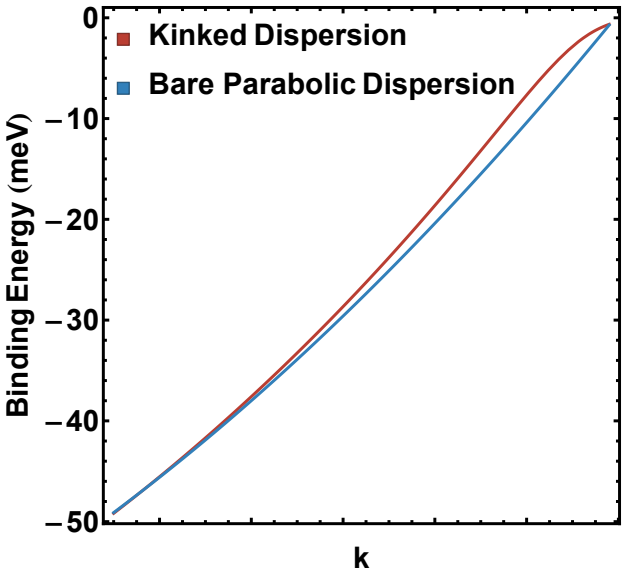

Figure 4.1: Schematic of a Kink in the Quasiparticle Dispersion

and $\epsilon^L(\mathbf{q},\omega)$ is the real part of the full longitudinal dielectric function comprising all longitudinal excitations arising from the Coulomb interaction in the solid.

There are a number of reasons to suggest that M-EELS is an appropriate probe to resolve the origin of these kinks, especially in the case of a coupling to a collective mode. Because ARPES is, similar to M-EELS, a surface sensitive spectroscopy, the many-body system studied using both probes is essentially identical. In addition, since the probe particle used in M-EELS experiments are electrons, they will couple to collective excitations in a similar way that electrons in the solid (i.e. the internal electrons) necessarily would. This correspondence is not expected to be perfect due to the surface potential, but the Coulomb interaction is expected to be the dominant interaction in the scattering process for both the probe electron and the internal electron. Below, the origin of the kinks is systematically studied in $Bi_2Sr_2CaCu_2O_{8+\delta}$, in Bi_2Se_3 and briefly in 2H-$TaSe_2$.

4.2 Collective Modes in $Bi_2Sr_2CaCu_2O_{8+\delta}$

The problem of cuprate superconductivity is one of the most pressing challenges in modern condensed matter physics. Significant progress on understanding the nature of superconductivity has been made since its discovery, with one of the most notable being the solution of the order parameter symmetry. In 1998, van Harlingen and co-workers, in a very elegant Josephson interference experiment, demonstrated conclusively that the order parameter for $YBa_2Cu_3O_{6+x}$was of the $d_{x^2-y^2}$ kind [42]. This implied that there was a sign-change in the orbital part of the order parameter and that there existed nodes associated with the gap function (though this was known before this landmark experiment).

Dispersion kinks along the nodal direction were first observed in $Bi_2Sr_2CaCu_2O_{8+\delta}$(Bi-2212) in 1999 and their first systematic study was undertaken in 2001 [38,43]. These original studies noted that the energy scale of the kink was between 50-80 meV and was surprisingly at the same energy scale for $La_{2-x}Sr_xCuO_4$and for two members of the Bi-based compounds (Bi-2201 and Bi-2212), suggestive of a common origin [38]. The kinks were observed both in the normal and superconducting state. It was more recently discovered that there also existed dispersion anomalies along the anti-nodal direction as well [44]. The presence of these kinks, along both nodal and anti-nodal directions, was highly suggestive of a coupling to a collective mode. It has even been suggested that the kink is a manifestation of a coupling to two collective excitations [45].

4.2.1 Data and Observations

Here, M-EELS was employed in attempt to elucidate the origin of these kinks. The spectra, shown in Fig. 4.2, were taken at 20 K in effort to confront the effects of thermal broadening with an incident beam energy of E_{inc} =7 eV. Spectra were also taken at 15^o and 30^o cuts from the anti-nodal direction. The altogether four cuts were taken at room temperature for comparison as well. Effects due to extra scattering in the elastic channel at low

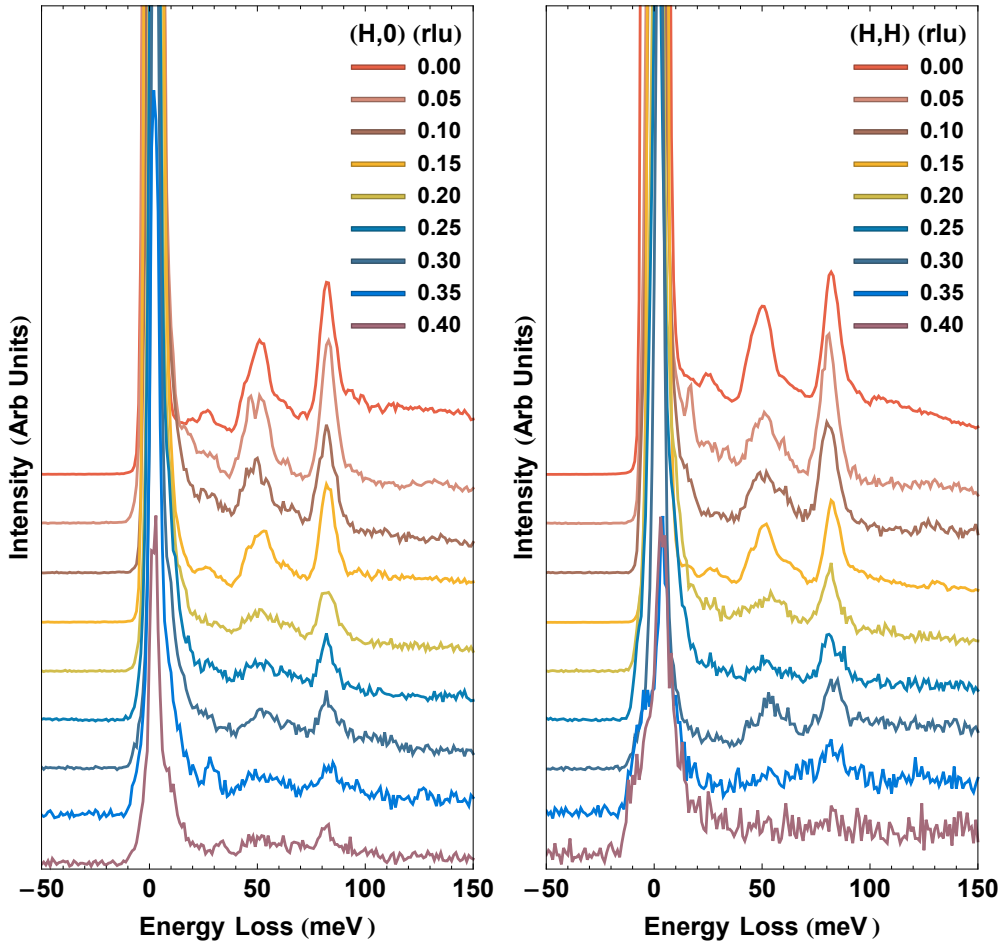

Figure 4.2: Raw M-EELS Spectra of Bi-2212 along the Anti-Nodal Direction (left) and the Nodal Direction (right) at 20 K

temperature were observed, but details related to these effects did not have a large bearing on the interpretation of the data with respect to the quasiparticle dispersion anomalies. The main features observed in the data are at ∼17 meV, ∼24 meV, ∼48 meV and ∼80 meV, indicating the presence of at least four collective modes. The modes are quite dispersionless and decay away toward the zone boundary, due to the fact that the scattering cross section weakens at large values of in-plane momentum transfer (see Eqs. 2.17-2.19).

4.2.2 Discussion and Analysis

The most notable detail of the spectra, plotted in Fig. 4.2, is the close correspondence between the energy of the stronger-intensity ∼48 meV and ∼80 meV modes and the energy scale of the ARPES kink. To explore further the possibility of whether the kinks are the origin of the dispersion anomalies, a more quantitative approach was taken. Tight-binding fits to the normal state band structure of Bi-2212 was taken from Ref. [46] and were renormalized using fits to the the M-EELS spectra. This procedure is described in detail in the supplemental section of Ref. [47]. However, this procedure can be adequately understood within the framework of Eq. 4.1. The calculation, with two fitting parameters, the Fermi velocity and the electron-phonon coupling constant (which was chosen to be a constant independent of momentum), resulted in the renormalized quasiparticle dispersion shown in Fig. 4.3. The Fermi velocity was chosen to be 2.5 eVÅto fit the high binding energy dispersion. This value is a little higher than the usually quoted value for Bi-2212, which is in the region of ∼1.8-2 eVÅ, but is not unreasonably large [48, 49]. It is reasonable to ask whether the procedure performed here is appropriate for the cuprate material class, as the existence of normal-state quasiparticles is even debated. The results of this calculation should therefore be understood within this context – the fit shown here should be taken to show the plausibility that these modes are together the origin of the ARPES kink.

There are two pressing questions that remain regarding these modes: (1) what are these features (e.g. phonons, magnons, etc.) seen in the M-EELS spectra? and (2) are the properties shown here characteristic of the bulk? It turns out, though, that these questions are not necessarily separable, as will be seen in the following discussion. The first question can be addressed by comparing with infrared spectroscopy data from Ref. [1] and with data taken on an underdoped (T_c ∼50K) as shown in Fig. 4.4. It is important to take into consideration that IR spectroscopy is a bulk-sensitive probe. That there is excel-

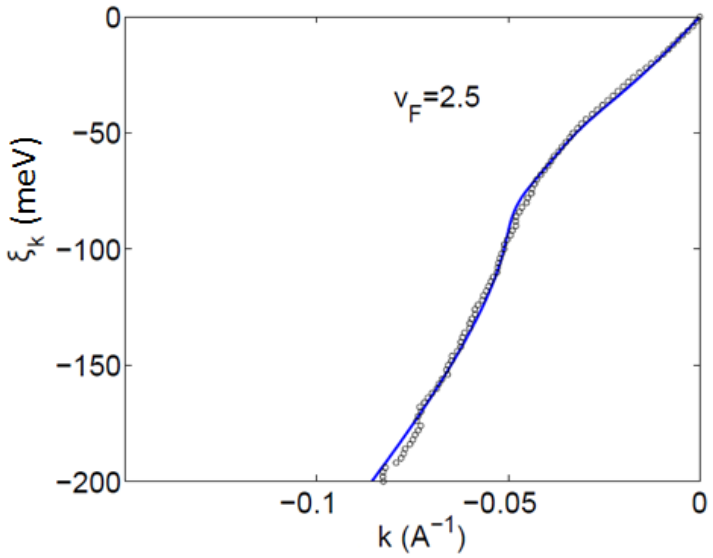

Figure 4.3: Fit to ARPES Quasiparticle Dispersion using Self-Energy Correction from M-EELS Data

lent agreement between the optimally doped IR spectrum and the **q**=0 optimally doped M-EELS data, apart from energy resolution effects, is not entirely surprising given the layered nature of the Bi-2212. What is surprising, however, is that the IR data presented here is for $\mathbf{E}||c$. Naively, one would think that the M-EELS spectrum would not match the c-axis (out-of-plane) IR response, but rather the a-b plane (in-plane) response. This discrepancy is likely due to screening effects, which starts to address the second question above. Before addressing that point, however, it is important to note the IR studies, with better energy resolution, demonstrate that multiple overlapping peaks are present around ∼48 meV. Moreover, the M-EELS spectrum demonstrates that one of these peaks is doping dependent, in that it shifts ∼3 meV between underdoped and optimally doped samples.

Now, we return to the question of screening effects. Depending on the penetration depth of the electrons, the electrons may not be adequately probing the Cu-O plane, as it is known that Bi-2212 is terminated by the Bi-O layer, followed by the Sr-O layer, upon cleaving. Only ∼4.7Ådown is the Cu-O layer, the plane in which the charge carriers re-

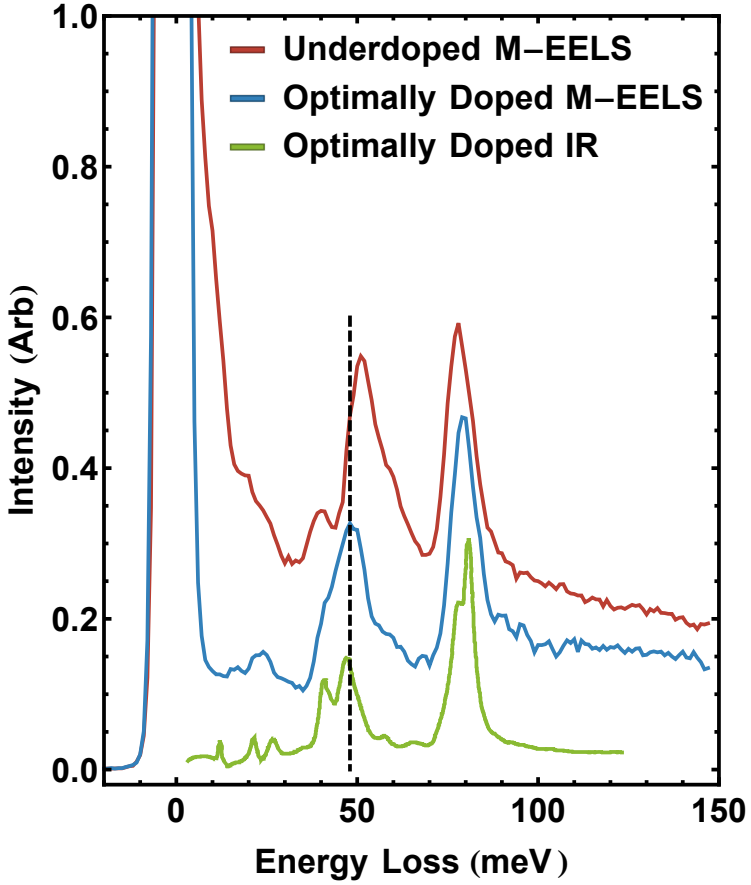

Figure 4.4: Comparison of E_{inc}=7 eV, **q**=0 M-EELS Underdoped (∼50K) and Optimally Doped (∼ 91K) Bi-2212 Specta with IR Optimally Doped c-axis Loss Function Spectrum. IR Data is taken from Ref. [1].

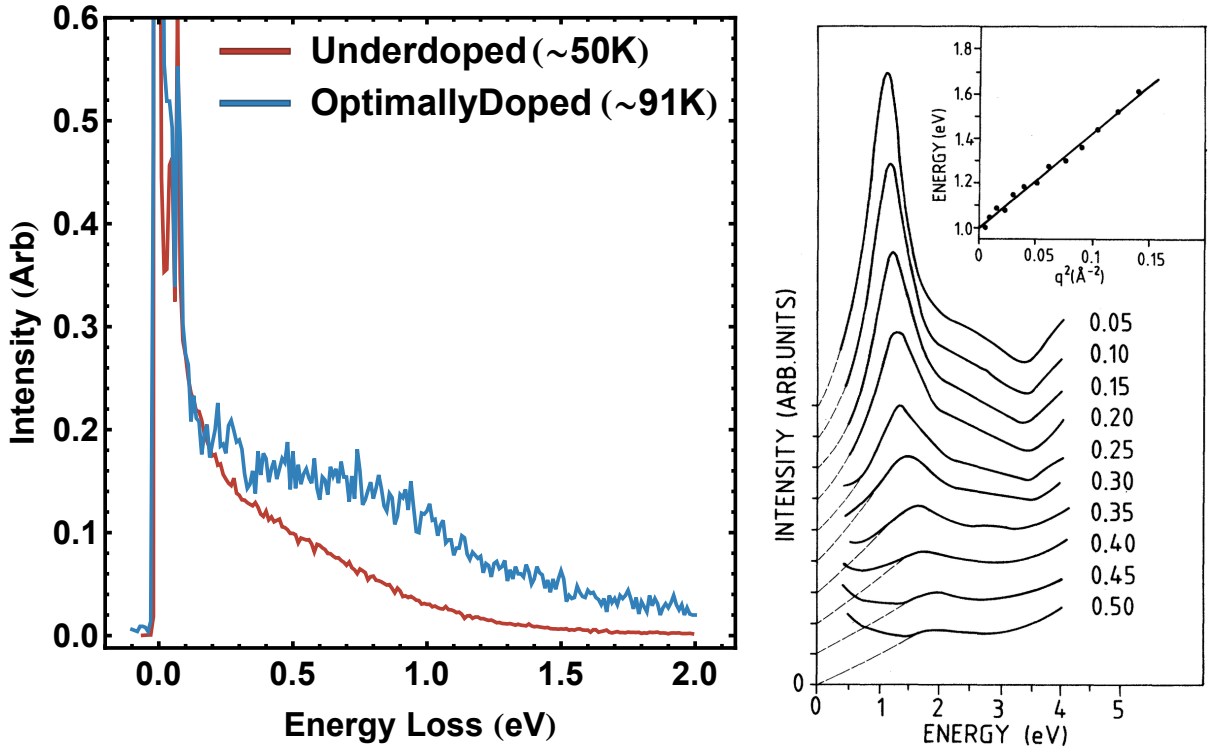

Figure 4.5: Comparison of E_{inc}=50 eV, **q**=0 M-EELS Spectra on Underdoped (∼50K) and Optimally Doped (∼ 91K) Bi-2212 (left) with Transmission EELS Spectra (right). Transmission EELS Data is taken from Ref. [2].

side. According to the "universal curve" of the electron inelastic mean free path, electrons at 7 eV are thought to have an inelastic mean free path of ∼15Å, while at 50 eV it is ∼3-5Å. To truly test whether M-EELS is probing the Cu-O plane, higher energy M-EELS spectra were taken at **q**=0 and compared to transmission EELS spectra, shown below in Fig. 4.5. The M-EELS spectra shown in the Fig. 4.5 was taken with E_{inc}=50 eV, but the spectra are similar for scans taken at E_{inc}=7 eV (not shown).

It is important to stress that the M-EELS spectra in this energy range is highly doping dependent, suggestive that the high energy scattering is sensitive to the presence of mobile charge carriers. However, when comparing to the transmission EELS spectra, it is clear that spectra are not in qualitative agreement [2]. It should also be reemphasized that the high-energy M-EELS spectra are also not in qualitative agreement with the in-plane IR data in this region, which instead agrees well with the transmission EELS data [1].

Together, these observations suggest that the M-EELS spectra are indeed sensitive to the charge carriers and probably to the Cu-O plane, but are screened by the outermost Bi-O and Sr-O layers in some way. In addition, they imply that the kink structure in the quasiparticle dispersion is likely due to these very phonons, which are also present in the bulk material. The doping-dependent behavior of the ∼48 meV phonon, and not the others, suggests a strong electron-phonon coupling to this mode, in favor of this view.

Lastly, as an aside, it should be noted that preliminary studies of the spectra at E_{inc}=200 eV show qualitatively similar high-energy spectra to that at E_{inc}=50 eV. This suggests that a quantitative analysis to compare the M-EELS spectra to the superconducting condensation energy as outlined in Refs. [14] and [15], while still possible, may require additional theoretical input to discern how to relate the spectra observed here to the Cu-O plane loss function. Therefore, an absolute test of the MIR scenario proposed in Ref. [14] and alluded to in the introductory material of this thesis, may require the use of transmission EELS or inelastic X-ray scattering.

4.3 Collective Modes in Bi_2Se_3

Two-dimensional topological insulators were discovered in 2007 in HgTe/(Hg,Cd)Te quantum wells and are characterized by a $\mathbb{Z}_2$ topological index [50–52]. In three-dimensions, topological insulators are characterized by four $\mathbb{Z}_2$ indices, one of which, usually denoted ν_0 determines whether a material is a strong topological insulator [53]. In 2009, Bi_2Se_3 was predicted and experimentally shown to be a three-dimensional topological insulator [54, 55]. Bi_2Se_3 falls into the category of strong topological insulators and is characterized by the presence of a single Dirac cone at its surfaces [55].

It has since been discovered that these surface states also possess a quasiparticle dispersion anomaly at ∼20 meV for low-carrier concentration samples [39, 40]. In these papers, the kinks were attributed to the presence of the out-of-plane A_{1g} phonon seen in

Raman studies, but there has not been a serious attempt in the literature to figure out the origin of the dispersion anomaly. Therefore, M-EELS was employed in attempt to figure out the origin of the kink structure in Bi_2Se_3. M-EELS studies of another topological insulator, $Bi_{0.5}Sb_{1.5}Te_{3-x}Se_x$ (BSTS), was also undertaken for comparison. Another reason for investigating these samples was the hope of observing the spin-plasmon mode predicted to exist in Ref. [18].

4.3.1 Data, Main Observations and Analysis

For this study, a number of Bi_2Se_3 samples were used with different Bi:Se growth ratios to combat selenium vacancies, which are known to be a source of bulk conduction in Bi_2Se_3 crystals [56]. The seven batches are labeled 1A-7A in ascending order of the carrier densities. Similarly, the seven batches of $Bi_{0.5}Sb_{1.5}Te_{3-x}Se_x$ crystals are labeled 1B-7B in ascending order of x.

Prior to performing M-EELS experiments, the crystals were characterized with angle-resolved photoemission at the Synchotron Radiation Center and the National Synchotron Light Source to determine the position of the Fermi energy relative to the bulk conduction bands and the surface Dirac band. For the Bi_2Se_3 materials, Fermi energies of some samples in batches 1A-3A were found to reside in the bulk gap. All of the samples from batches 4A-7A were observed with the Fermi energy in the bulk conduction band, as illustrated in Fig. 4.6(a)-(c). This is consistent with previous findings under similar growth conditions [56]. Samples from batches 3B-7B were found to be p-type with respect to the Dirac surface bands and the bulk valence band. The Fermi energies in batches 1B and 2B were found to reside in the bulk gap and very close to the Dirac point, as shown in Fig. 4.6(d)-(f), with only slight sample-to-sample variation in the Fermi energy.

For the M-EELS measurements, the samples were cleaved *in-situ* in a vacuum of $<5\text{x}10^{-10}$ Torr. The spectra were taken within 30 minutes of the cleave unless stated

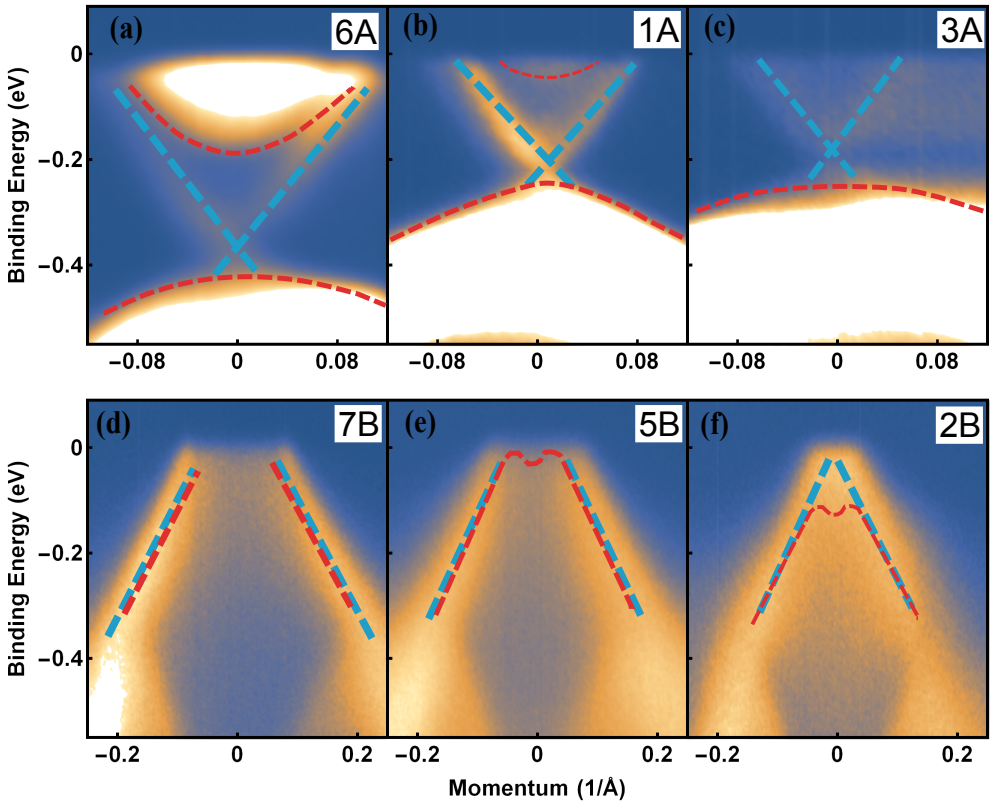

Figure 4.6: (a)-(c) ARPES spectra taken at 55K of Bi_2Se_3 from sample batches 6A, 1A and 3A respectively. (d)-(f) APRES spectra taken at 20K of BSTS from batches 7B, 5B and 2B respectively. Lines are drawn to guide the eye. Blue dashed lines indicate the surface Dirac bands while the red dashed lines indicate the bulk bands.

otherwise. The typical energy resolution for these experiments was ∼10 meV while the momentum resolution was 0.04 $Å^{-1}$ The incident beam energy was 50 eV for all measurements taken.

M-EELS measurements are shown in Fig. 4.7. In both the Bi_2Se_3 and BSTS cystals, a high-intensity inelastic feature was observed (Fig. 4.7(a) and (b)). The data in Bi_2Se_3 were taken at room temperature, while the data in BSTS were taken at 100K. The most pronounced aspect of the peak in Bi_2Se_3 is its dependence on the bulk carrier density. As the n-type carrier density is tuned from 2×10^{19} cm^{-3} to 1.2×10^{18} cm^{-3}, there is a pronounced shift in the peak energy from ∼90 meV down to ∼23 meV, identifying this mode as a collective excitation of the valence electrons, i.e., a free carrier plasmon. In the BSTS materials, a similar plasmon peak was also observed between 30-34 meV for all samples examined. Though there is slight variation in the peak energy from sample to sample, the variation is not monotonic with the sample composition, so likely occurs due to different vacancy concentrations in the samples. Most importantly, the peak energy is insensitive to the location of the Fermi energy relative to the Dirac point, but correlates instead with the bulk carrier density (Fig. 4.9(a)). This suggests that this excitation is a plasmon-like mode that derives from the free carriers of the bulk, rather than the Dirac surface states.

The strength of the coupling of this boson to the electrons can, in the first approximation, be characterized by the magnitude of $\chi''(\mathbf{q}, \omega)$, which enters the lowest-order correction to the electron self-energy [5]. From Fig. 4.7(a), it is clear that, in the energy range examined, the largest contribution to the spectral weight of $\chi''(\mathbf{q}, \omega)$ comes from the plasmon. This is consistent with a significant electron-plasmon coupling and suggests that this excitation is likely to renormalize the quasiparticle dispersion at ∼20 meV in Bi_2Se_3 for low carrier concentration samples.

To characterize the dependence of the mode on surface quality, time-dependent data were taken for Bi_2Se_3, summarized in Fig. **??**(b). A spectrum from a sample from batch

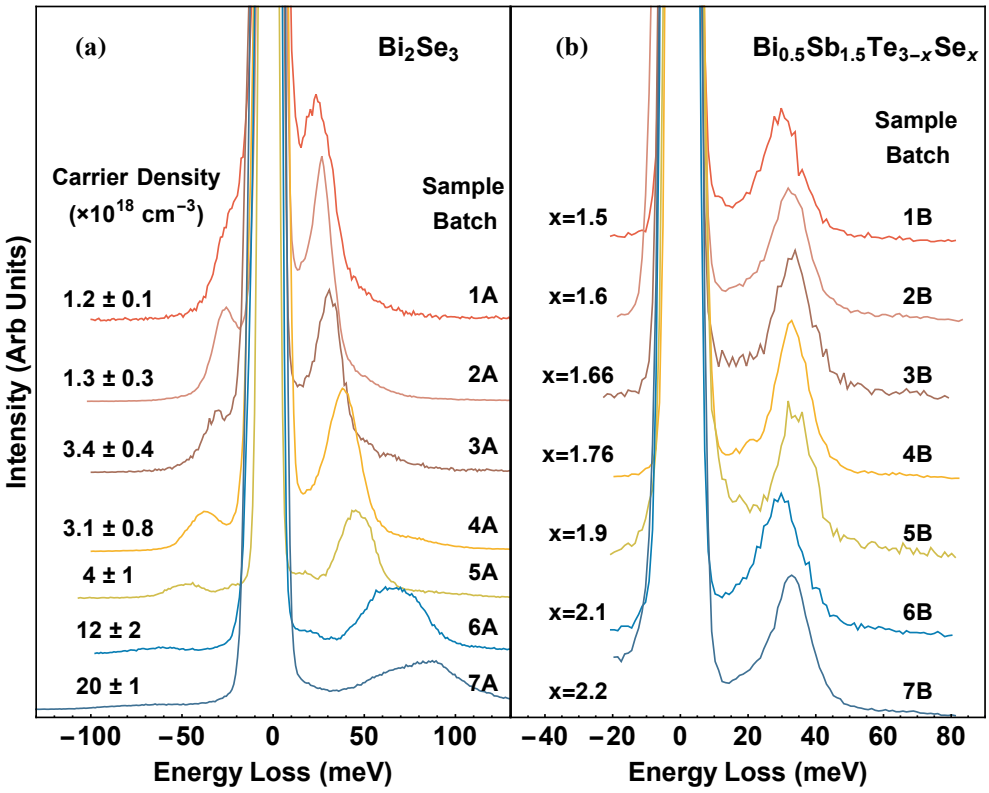

Figure 4.7: (a) M-EELS spectra at **q**=0 showing the plasmon dependence of the plasmon peak on the carrier density in Bi_2Se_3 at room temperature. (b) M-EELS spectra at **q**=0 showing the lack of dependence of the plasmon on the location of the Fermi energy with respect to the surface Dirac bands in BSTS at 100K. Spectra are displaced vertically for ease of view.

6A, which is observed to have a plasmon at 65 meV about a half-hour after cleavage, undergoes a drastic change with time. In a period of 24 hours, the plasmon peak shifts in energy by about 25 meV to 90 meV, yielding a spectrum that resembles a sample from batch 7A, which, nominally, is much more highly electron doped. This data is consistent with observations in ARPES in which the bands were seen to bend at the surface, leading to increased electron doping as a function of time under ultra-high vacuum conditions [55]. Time-dependent measurements were also conducted on Bi_2Se_3 from batch 3A, shown in the inset of Fig. **??**(b). Again, a shift in the peak energy of about 15 meV was observed in the 46-hour period of time examined. This data establishes that the excitation studied here, while deriving from the free carriers of the bulk, is nevertheless highly dependent upon the properties of the surface, which evolve in time in essentially the same manner as observed by ARPES studies [55]. Put together, all preceding evidence suggests that the excitation is a conventional surface plasmon arising from the same free carriers that cause bulk conduction.

To probe its propagation characteristics, the dispersion of the surface plasmon was measured for both sample families. In Fig. **??**(a), data from batch 3A in Bi_2Se_3 is shown (the data from BSTS yielded very similar results). One can see that there is no observable dispersion in this mode in the momentum region examined. Dispersion data was also taken on highly doped samples with similar results. This is consistent with our identification of this mode as a surface plasmon: In the standard electromagnetic theory, a surface plasmon disperses from zero energy with a phase velocity close to the speed of light, and saturates at energy $\omega_p/\sqrt{2}$ [57]. For the plasmon studied here, $q_s \sim 8 \times 10^{-6}\text{Å}^{-1}$, which is far below our momentum resolution of $\Delta q = 0.03\text{Å}^{-1}$. Hence, one expects a single, non-dispersive peak at $\omega_p/\sqrt{2}$, which is what is observed here.

This mode assignment can corroborated by comparing the energy dependence of the surface plasmon to the measured carrier density for Bi_2Se_3. The bulk plasmon has fre-

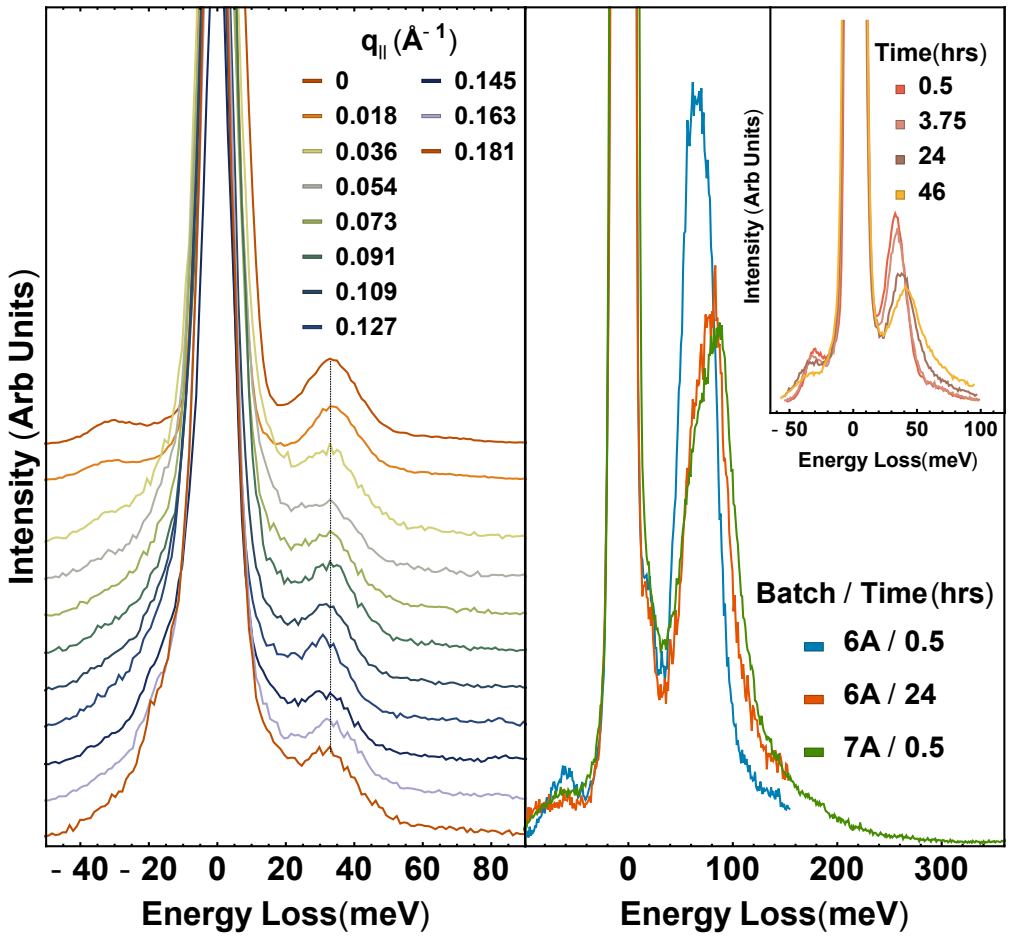

Figure 4.8: Left: Dispersion of the plasmon taken at room temperature from a Bi_2Se_3 sample from Batch 3A. Right: Time dependence of a Bi_2Se_3 sample from Batch 6A compared to a freshly cleaved sample from Batch 7A. Inset: time-dependence of Bi_2Se_3 sample from Batch 3A.

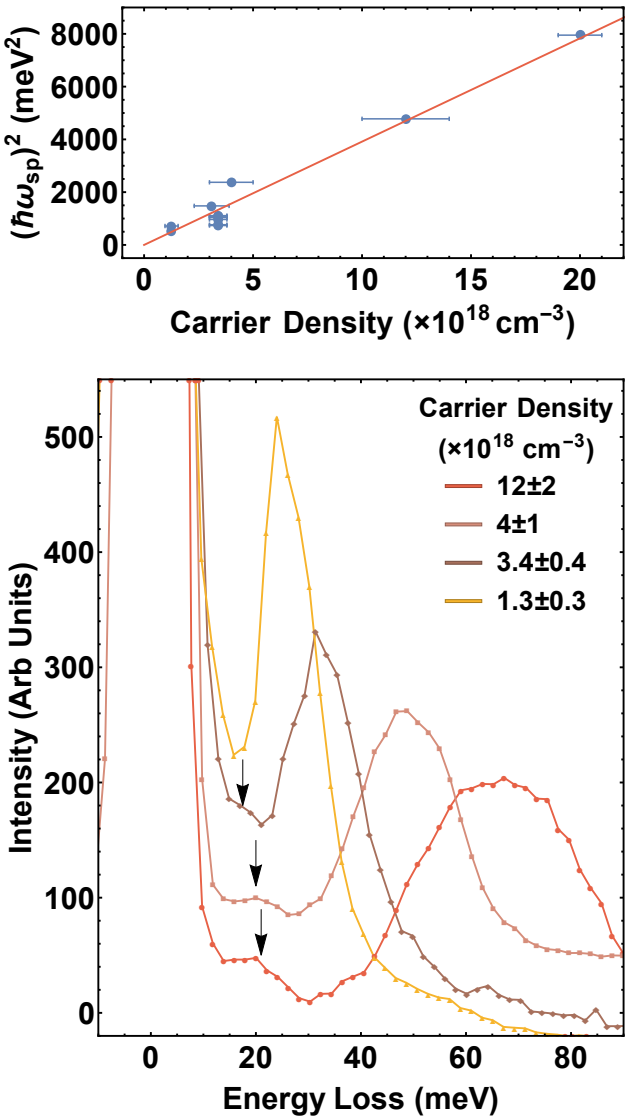

Figure 4.9: Top: Squared surface plasmon energy as a function of carrier density determined from Hall measurements. Bottom: Observation of a low energy collective mode, which is the surface analog of the out-of-plane A_{1g} phonon.

quency (in SI units):

$$\omega_p^2 = \frac{ne^2}{\epsilon_0 \epsilon_\infty m^*} \tag{4.3}$$

where e is the electron charge, m^* is the effective mass and ϵ_∞ is a background constant representing the contribution of high-energy interband transitions, not measured in our experiment, to the full dielectric function, $\epsilon(\omega)$. The surface plasma frequency is related to the bulk plasmon using the relation [58]:

$$\omega_{sp}^2 = \frac{\epsilon_\infty}{\epsilon_\infty + 1}\omega_p^2. \tag{4.4}$$

By fitting a line to a plot of $\hbar^2\omega_{sp}^2$ against the carrier density, n, and performing a least-squares linear fit (see top panel of Fig. 4.9), a value of ϵ_∞=26$\pm$2 was extracted. This is a reasonable value for the background dielectric constant which is usually quoted to be between 25-29 [59–61]. Finally, the relation between the plasmon energy and the bulk carrier density in Fig. 4.9(a) appears to obey a square-root relation to a high accuracy, providing further evidence for this identification. It should be emphasized that for this relation to be valid, the plasma frequency must be measured within a short time-frame after cleaving the sample.

We can also use this fit to estimate the expected kink energy in a similar compound, $Cu_xBi_2Se_3$. Using the experimental Fermi energy from Ref. [41] of 250 meV, one expects a carrier density of 2.7$\pm$0.8$\times10^{19}$ cm^{-3}, implying a surface plasma frequency of 102$\pm$10 meV. This value is consistent with Refs. [41] and [62], in which a kink was observed at $\sim$90 meV. The lack of other excitations in this energy range is strongly suggestive that the surface plasmon is also responsible for the kink in $Cu_xBi_2Se_3$.

Interestingly, at high doping levels, a second collective mode is observed in Bi_2Se_3 (Fig. 4.9(b)). This mode has a much smaller spectral weight than the surface plasmon, but it also falls within the energy scale of the observed kink in low carrier density Bi_2Se_3 samples. This mode is most likely the out-of-plane A_{1g} phonon previously observed in

Raman scattering studies [59, 63]. That the energy of the mode shifts with carrier density and is not visible in the regime of lower carrier density suggests that this phonon mode is coupled in a non-trivial way to the surface plasmon and may form a composite excitation.

One may wonder whether we have seen any evidence for the spin plasmon, i.e., a collective mode of the Dirac surface states predicted by Ref. [18]. Unfortunately, it may not be possible to observe this excitation with existing EELS techniques. As we have shown, in real materials the surface response functions are dominated by scattering from bulk free carriers, rather than the surface states. Even if the bulk free carriers could be eliminated, however, the Dirac mode would still be nearly impossible to see. Even at the highest possible doping, $\mu \sim 0.3$ eV, the critical momentum of the plasmon $q_c \sim 4 \times 10^{-3}\text{Å}^{-1}$, lies below the momentum resolution of EELS techniques, so the Dirac plasmon would be overdamped in all spectra. A more fruitful approach might be scanning, near-field optical techniques, in which lower momentum scales can be accessed by studying the response functions is real space.

In summary, the collective modes on the surface of two topological insulators were studied and it was found that the primary feature is a surface plasmon arising from the free carriers in the bulk. Because of its large spectral weight contribution to $\chi''(\mathbf{q}, \omega)$, the surface plasmon is most likely the origin of the quasiparticle dispersion kinks at 20 meV and 90 meV observed with ARPES in Bi_2Se_3 and in $Cu_xBi_2Se_3$. It is therefore concluded that the kink is electronic in origin and might be tunable by varying the bulk carrier concentration.

4.4 Preliminary Results on 2H-$TaSe_2$

In a preliminary, but important undertaking, 2H-$TaSe_2$, a prototypical quasi-2D transition metal dichalcogenide (TMD) charge density wave (CDW) material was also examined. The reason for this study, was to provide further credence to the correspondence

between peaks observed in M-EELS spectra and dispersion anomalies observed in ARPES spectra. 2H-$TaSe_2$ undergoes two CDW transitions, one at 122 K and another at 90 K. The higher temperature transition corresponds to a transition to an incommensurate CDW state, while the lower transition corresponds to a 3×3 commensurate CDW state. It has been observed in Ref. [13] that there is a pronounced anomaly that develops in the quasiparticle dispersion once the system enters the CDW state. This is also manifested in a peak in the real part of the quasiparticle self-energy at $\sim$70 meV at $\sim$34K, the lowest temperature at which data was taken [13]. The peak in the real part of the self-energy was also seen to increase in energy as a function of decreasing temperature, from $\sim$30 meV at 111 K to $\sim$70 meV at $\sim$34K. The kink was believed not to arise from phonons because of the energy scale (the highest energy phonons are at $\sim$40 meV in this material) and because of the temperature dependence [13].

Thus preliminary M-EELS data was taken on this compound in effort to observe origin of this quasiparticle dispersion anomaly. The M-EELS spectra were taken with an incident beam energy of 50 eV. The data are shown in Fig. 4.10 comparing $\mathbf{q}$=0 spectra at 20 K and 300 K. It was indeed observed that a peak developed in the M-EELS spectrum at low temperature, confirming the prediction made by Ref. [13]. Though preliminary, this result provides a convincing demonstration of the correspondence between kinks seen in ARPES spectra and the observation of corresponding collective modes in M-EELS spectra.

4.5 Conclusion

To conclude this chapter, it should be emphasized that, because of the energy and momentum ranges accessible to M-EELS, the possibility of resolving questions concerning the origin of quasiparticle dispersion anomalies often seen in ARPES studies can start to be addressed in a more convincing fashion. Because M-EELS uses electrons as a probe, and the interactions are expected to be similar for an 'internal' electron, the cross-section

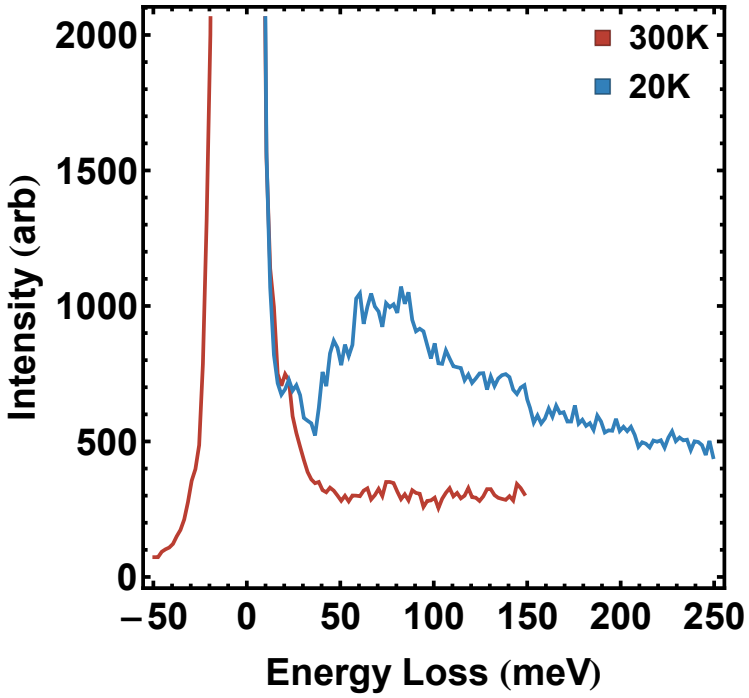

Figure 4.10: **q**=0 M-EELS Spectra of 2H-$TaSe_2$ at 20 K and 300 K

can yield important insights into the collective modes likely to give rise to dispersion kinks. These dispersion anomalies are indicative of many-body effects in the solid, which may be important in systems that undergo transitions to a broken symmetry ground state. The development of M-EELS as a detector of the origin of dispersion kinks paves the way forward to enhancing our understanding of many-body effects in solids and the coupling of quasiparticles to collective modes leading to the formation of unusual ground states.

Chapter 5

Electronic Excitations in 1T-$TiSe_2$

5.1 $TiSe_2$ and the Excitonic Insulator Phase

1T-$TiSe_2$ is a transition metal dichalcogenide (TMD) that, since the mid-seventies, has been known to host a charge density wave (CDW) transition [64]. The transition is characterized by a 2x2x2 superlattice formation at 202 K [64]. The structure of this compound is hexagonal and is part of the 1T polytype family characteristic of many TMDs. The structure is shown schematically in Fig. 5.1. The c-axis is van der Waals bonded, making this sample easy to cleave and ideal for M-EELS studies.

$TiSe_2$ has remained a controversial material for many decades due to speculations about the origin of the CDW transition. Unlike many other TMDs that undergo a CDW transition (e.g. 2H-$NbSe_2$, 2H-$TaSe_2$, 2H-TaS_2 and 1T-TaS_2), $TiSe_2$ does not have an intermediate state where the CDW is incommensurate [65, 66]. Notably, also, $TiSe_2$ is either a narrow bandgap semiconductor or a small-overlap semi-metal in its 'normal' phase [3,67,68]. These two facts have led to the speculation that at low temperature, $TiSe_2$ is actually an excitonic insulator, though this is debated [25]. The mechanism behind the CDW transition in $TiSe_2$ has been speculated to arise from numerous other origins as well including anisotropic electron-phonon coupling, a band-type Jahn-Teller effect and Fermi surface nesting [23, 25, 67]. In the past few years, however, there has been an emerging consensus that both excitonic effects and electron-phonon coupling are important [69–72].

At this point, a quick overview of the excitonic insulator state is apt. There are two limits from which the formation of this state of matter can be considered. These are the

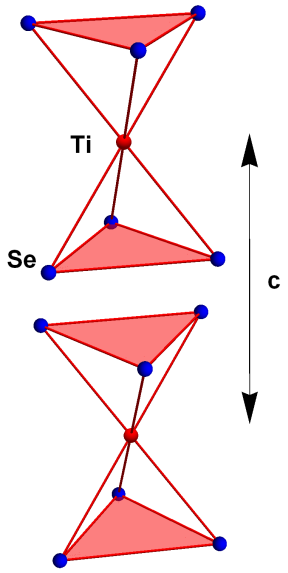

Figure 5.1: 1T structure of $TiSe_2$

semiconducting and the semimetallic limits. A heuristic understanding of the excitonic insulator state can be obtained in the following way. First, we consider the semiconducting limit with an indirect band gap pictured schematically in Fig. 5.2 (left).

It is known that for such a system, the lowest energy electronic excitation is an exciton (a bound electron hole pair) with a binding energy, E_B, which is generally smaller than the gap energy, E_g. However, if one can imagine decreasing the gap energy by tuning E_g, there will be a point where E_B will become greater than E_g. At this point, the semiconductor is unstable to the spontaneous formation of excitons and will collapse into a new ground state denoted an excitonic insulator [73].

One can also reach the excitonic insulator ground state by appealing to the opposite limit of a small negative gap semimetal (i.e. $E_g < 0$), which is shown in Fig. 5.2 (right). This limit was first considered by Mott and is related to screening effects [74]. Here, one can imagine that the plasmon associated with the semimetallic state decreasing in energy as the E_g approaches zero. However, before E_g reaches zero, there is a characteristic energy scale, $E_1 < 0$, above which the carrier density becomes so low that electron-hole

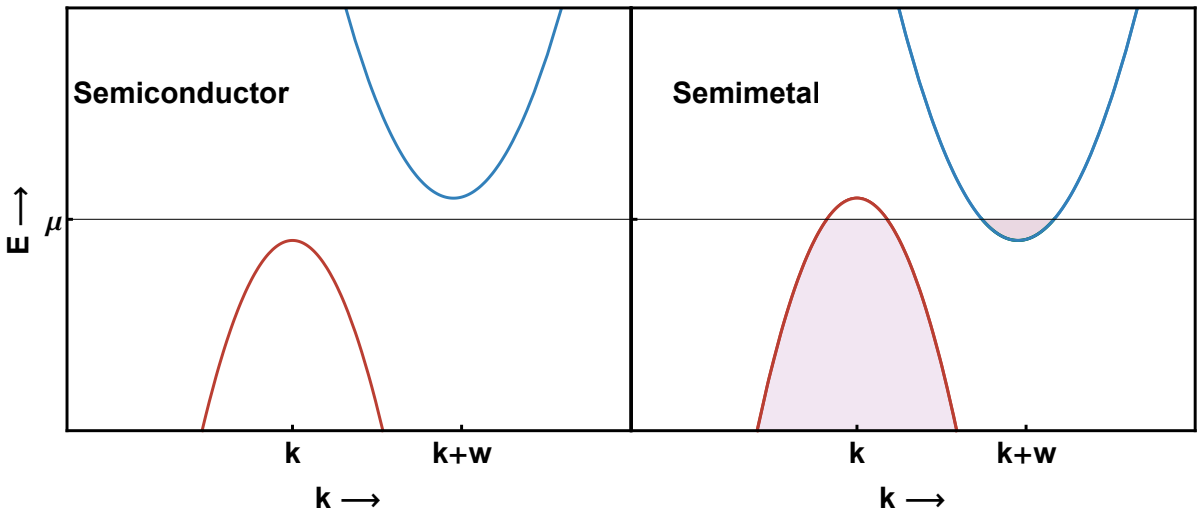

Figure 5.2: Schematics of normal state band structures unstable to the formation of an excitonic insulator groundstate. (Left) Small indirect gap semiconductor. (Right) Small overlap semimetal.

pairs are no longer sufficiently screened. Therefore the formation of bound electron-hole pairs becomes energetically favorable leading to localization and the formation of the excitonic insulator ground state.

When considering a structural or lattice instability associated with a charge density wave transition, there are usually one or more phonon modes that are seen to soften at the transition temperature, T_c [7, 23]. Analogously, it can be said that at the transition to the excitonic insulator state one expects to see a 'soft exciton' or a 'soft plasmon' associated with the transition, depending on whether the excitonic insulator ground state is approached from the semiconducting or the semimetallic limit. This softening should occur at the wavevector, w, that connects the bottom of the conduction band to the top of the valence band [27]. The distinction between a plasmon and an exciton in this limit may be largely semantic, however, as both modes consist of electron-hole pair excitations. It should also be kept in mind that as the plasmon or exciton softens toward zero energy, that the electronic branch will necessarily hybridize with a phonon branch of identical

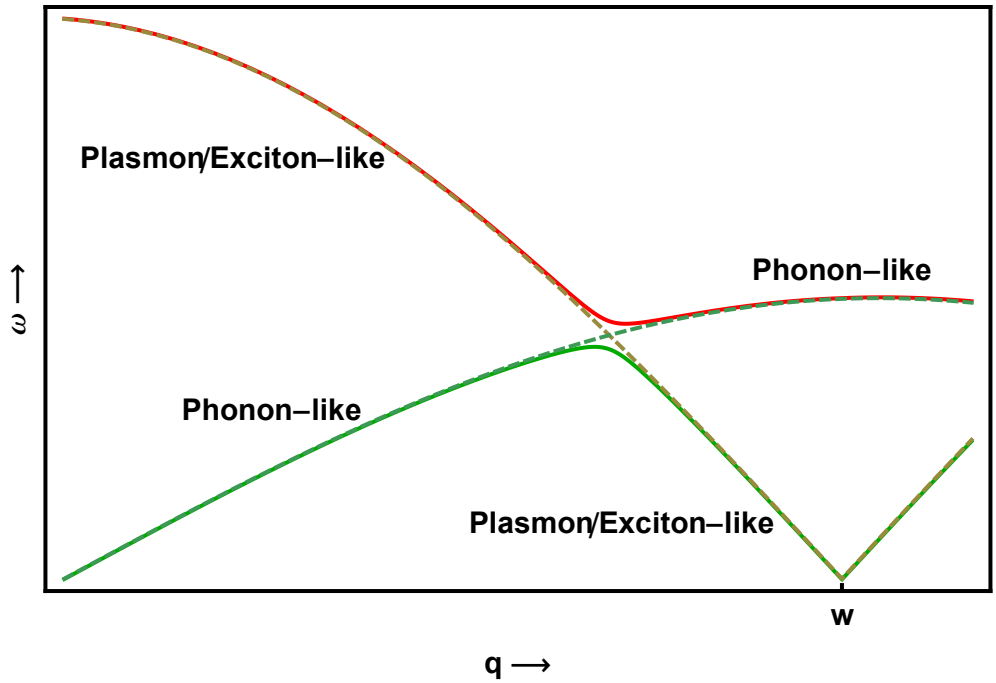

Figure 5.3: Collective modes near the transition to the excitonic insulator state.

symmetry. Therefore, while the driving mechanism of the excitonic insulator state will be largely electronic in origin, a lattice instability will also accompany the transition due to the phonon-plasmon/exciton mixing [27, 73]. Obviously, the degree of mixing between these two branches will ultimately determine the degree to which the lattice distorts as a result of the transition to the new ground state. A schematic of this idea is shown in Fig. 5.3.

While a soft plasmon/exciton branch is expected to occur at the transition to an excitonic insulator, this is by no means the only property associated with the ground state. If the wavevector, w, of the transition happens to be incommensurate with the underlying lattice, it is expected that a translation of the electron-hole condensate will cost no energy, leading to a collective excitation denoted an "excitonic sound" wave [27]. This mode is expected to have a linear dispersion at long wavelengths. This collective mode is analogous to the phase mode seen in charge density wave systems [7]. It should be noted, though, that there exists a subtlety associated with the dispersion of the "excitonic sound" wave.

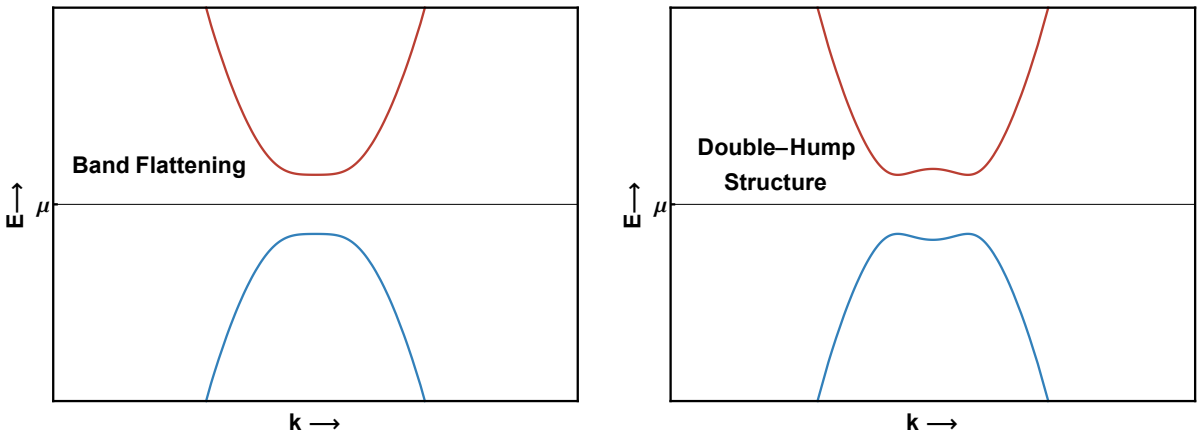

Figure 5.4: Band structure expected in the excitonic insulator state after zone-folding.

Because it is a collective mode of charged particles and screening is expected to be weak, the long-range nature of the Coulomb interaction may lead to an energy cost associated with the mode even in the long-wavelength limit. An energy cost in the long-wavelength limit is also expected to occur for an excitonic insulator with a commensurate wavevector, similar to the phase mode in common CDW systems [7]. The ground state of the excitonic insulator phase is further typified by a gap in the single-particle spectrum and a characteristic flattening/repulsion associated with the conduction and valence band extrema associated with zone-folding, shown schematically in Fig 5.4. To recapitulate, the excitonic insulator transition is characterized by (at least) five main experimentally observable properties: (1) A soft plasmon/exciton at T_c at the wavevector, w, connecting the conduction and valence band extrema, (2) a new collective mode associated with the excitonic condensate, (3) the opening of a gap in the single-particle spectrum, (4) a flattening or double-hump structure at the valence and conduction band extrema and (5) a small-gap semiconducting or small-indirect-overlap semimetallic normal state. It should also be emphasized that the excitonic insulator ground state has been shown not to possess the quality of off-diagonal long range order (ODLRO) characteristic of superfluid systems [27,73].

5.1.1 Brief Overview of the Current Experimental Status

Before delving into our experimental results, it is necessary to understand the current experimental status surrounding $TiSe_2$. Of the five criteria listed above, the opening of the gap in the single-particle spectrum is the most well-established experimentally using angle-resolved photoemission spectroscopy [69,71,72,75,76]. Though there is debate about the exact value of this single-particle gap, at low temperatures, most quoted values fall within ∼65-100 meV [25]. At high temperatures, the nature of the normal state is debated. Whether $TiSe_2$ is a small-indirect-overlap semimetal or a small-gap semiconductor has been discussed extensively, though it should be reemphasized that both these normal states are unstable to the excitonic insulator ground state [25, 67]. The double-hump structure at the bottom of the conduction band is also established experimentally and is apparent in ARPES data from several disparate groups [67, 72, 76]. This is most clearly visible along the $L \rightarrow A$ direction in the Brillouin zone. Because these described effects can be observed with ARPES, they are the most well-established experimentally.

Much less is known however, about the collective excitations. On this front, there have been only a handful of pertinent studies [3, 23, 75, 77, 78]. An inelastic X-ray scattering experiment and an X-ray thermal diffuse scattering experiment have separately demonstrated the complete softening of a zone-boundary phonon at T_c [23, 75]. These were important studies showing that, even though it may still be an excitonic driving mechanism behind the transition, there is a substantial lattice component associated with the instability [23]. This interpretation has been further corroborated by a recent ultrafast THz study [77]. On the electronic side, as opposed to the structural front, two optical studies have demonstrated a startling change in the plasmon characteristics as a function of temperature [3,77]. Above T_c, the plasmon is broad and seemingly quite damped, while below T_c, the peak sharpens markedly [3]. Moreover, as the sample is cooled, the plasmon decreases in energy noticeably at $\mathbf{q}$=0 when approaching T_c and then increases

in energy below T_c. Though it is difficult to draw a strong conclusion from these studies, as they are confined to the Brillouin zone center, it is suggestive that something non-trivial is occurring to the electronic collective modes below T_c.

There is one more set of studies worth noting, though they do not directly address the criteria outlined above. These are the time-resolved studies that have demonstrated the melting time of the charge density wave state in $TiSe_2$ [69, 71, 77]. In these studies it was shown that the time-scale for CDW melting was below what would be expected of a typical Peierls-type electron-phonon driven transition. The melting time was compared to that of 1T-TaS_2, which is known to host both a Mott transition and a Peierls transition, for which the melting times differ markedly [71]. These studies are also suggestive of an electronic component to the CDW origin in $TiSe_2$, though again, they are not conclusive.

Lastly, in the original $TiSe_2$ studies, it was found that the transition temperature into the CDW state was extremely sensitive to crystal purity [64]. It was found that trace contaminants, which reduced the hole concentration and increased the electron concentration, could change T_c by as much as 10 K. The stoichiometric samples with highest T_cs were found to have an electron and hole concentration of approximately 10^{20} cm^{-3}. The authors therefore attributed the formation of the CDW in $TiSe_2$ to electron-hole coupling [64].

5.2 Experimental Observations

As has been stressed repeatedly in this thesis, it is important to address whether or not M-EELS measures the bulk spectrum in the materials investigated. On this front, the optical study in Ref. [3] was extremely important in establishing this relationship. The M-EELS spectra, taken at the Brillouin zone center, can be seen in Fig. 5.5. The spectrum from Ref. [3], obtained from a Kramers-Kronig analysis of reflectivity data, is shown for comparison in Fig. 5.6. The spectra clearly bear a strong resemblance to one another,

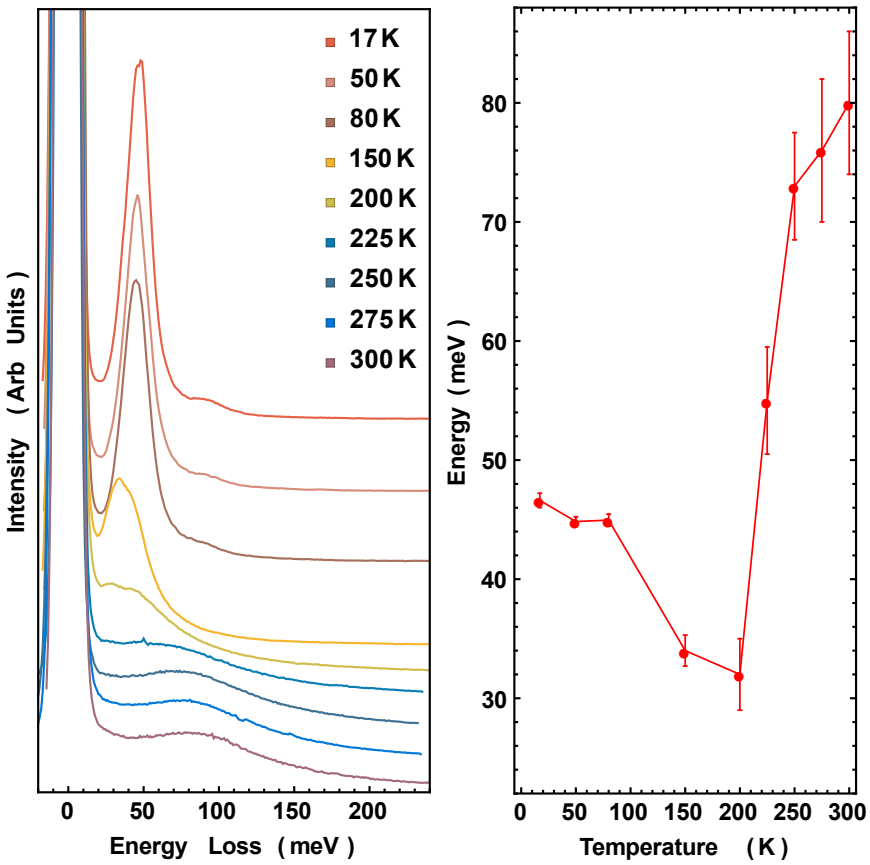

Figure 5.5: (Right) Temperature dependence of **q**=0 $TiSe_2$ energy loss spectrum. (Left) Peak position as a function of temperature.

firmly indicating that the in-plane surface response and the in-plane bulk response in $TiSe_2$ are indeed almost identical. This result also establishes that the cross-section for this material is closely related to the in-plane bulk loss function. Since the in-plane response is the quantity that is sought for $TiSe_2$, this is an extremely significant outcome.

Armed with this result, it is interesting to ask how the observed excitation disperses along different momentum directions at various temperatures. As a preliminary step to doing this, however, we oriented our sample *in-situ* to observe the CDW Bragg peaks at 100 K with an incident beam energy of 50 eV, as shown in Fig. 5.7. It should be emphasized again that because our technique is surface-sensitive, the out-of-plane momentum component is not conserved and therefore the Bragg peaks are indexed with only two Miller indices, (H,K). Both the (1/2,0) and the (1/2,1/2) Bragg peaks are clearly observ-

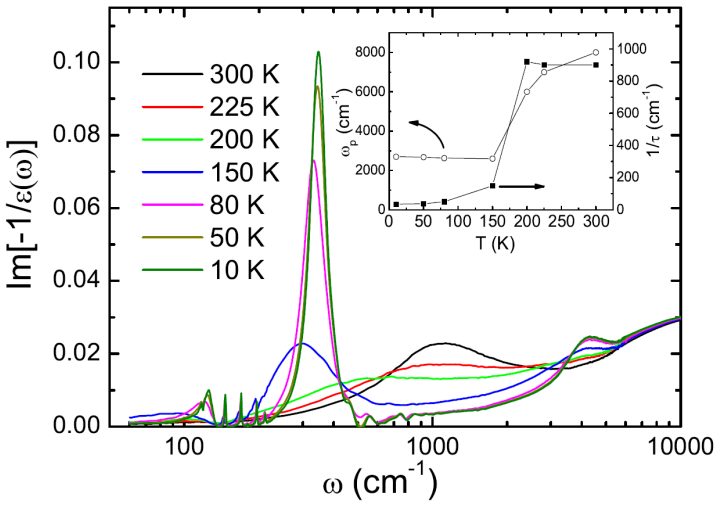

Figure 5.6: Loss spectrum of $TiSe_2$ obtained from Kramers-Kronig analysis of reflectivity. Reprinted with permission from American Physical Society [3].

able, which is consistent with the 2x2x2 modulation in the bulk sample. It is clear from these plots that, because of structure factor effects, the (1/2,0) peak is significantly weaker in comparison to the (1/2,1/2) peak.

5.2.1 Summary of Data Taken Along the (1,0) or $\Gamma \rightarrow M$ Direction

Having oriented the sample adequately, spectra were taken along the (1,0) ($\Gamma \rightarrow M$) direction at several temperatures with an incident beam energy of 50 eV. The raw spectra for 300 K and 185 K are shown below in Fig. 5.8. Two different sets of data were taken at 100 K and are shown in Fig. 5.9. The left panel of Fig. 5.9 was taken with double the collection time compared to the plot in the right panel. It should be noted, though, that while the spectra are less noisy in the left panel, adsorbates also have more time to collect on the sample surface for longer collection times. Therefore, it should be kept in mind that the data in the left panel was taken in reverse order from (1,0) to (0,0), with the idea that the high-**q** spectra are likely more reliable than the low-**q** spectra. The reader should also note the change in the x-scale when comparing raw scans at different temperatures. Because the highest-energy excitation is most pronounced well below T_c, as seen in Fig. 5.5,

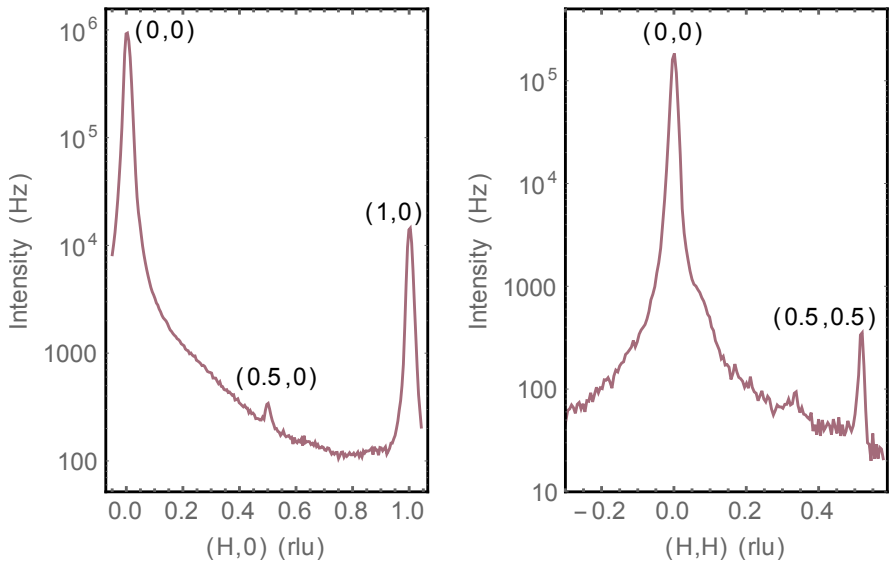

Figure 5.7: Bragg peaks at 100 K in the CDW phase.

the dispersion is the clearest in the 100 K data set. In the 100 K data set, one primary inelastic feature was identified and an example of the fitting procedure is shown for H=0.3 in Fig. 5.10. The elastic peak was fit with a pseudo-Voigt function, while the inelastic feature was fit with a Lorentzian. At 185 K the high energy feature was again the only mode identified. At 300 K, however, a broad peak was seen at ∼88 meV and another feature appears at higher energy for large **q**. This feature can be most clearly seen for H=0.5-1 in Fig. 5.8, where there is a marked change in the inelastic spectrum while scanning through **q**. Only fits to the lower energy mode are shown in Fig .5.11.

The dispersion of the peaks along the (1,0) direction at different temperatures are presented in Fig. 5.11. There is a noticeable dispersion in the inelastic feature towards the CDW wavevector at (1/2,0) below T_c. Looking at the left panel of Fig. 5.11, it is important to note that at low temperature, the spectra at (1,0), (0,0) and (1/2,1/2) are identical, but differ from (1/2,0) even though these are all Bragg points in the CDW phase. This occurs because of the structure factor leading to a weak CDW Bragg peak at (1/2,0), as

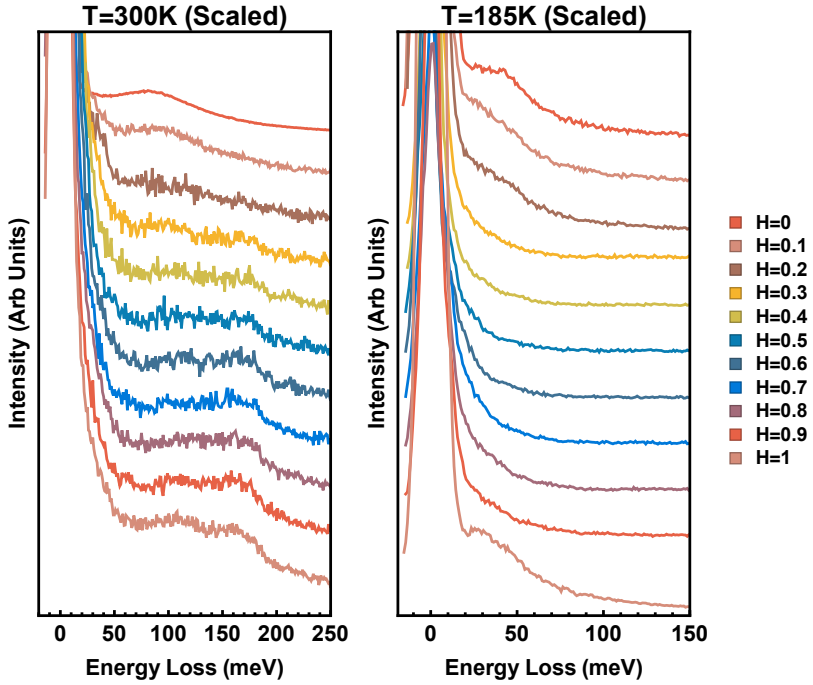

Figure 5.8: Raw M-EELS scans along (H,0) at 300 K and 185 K.

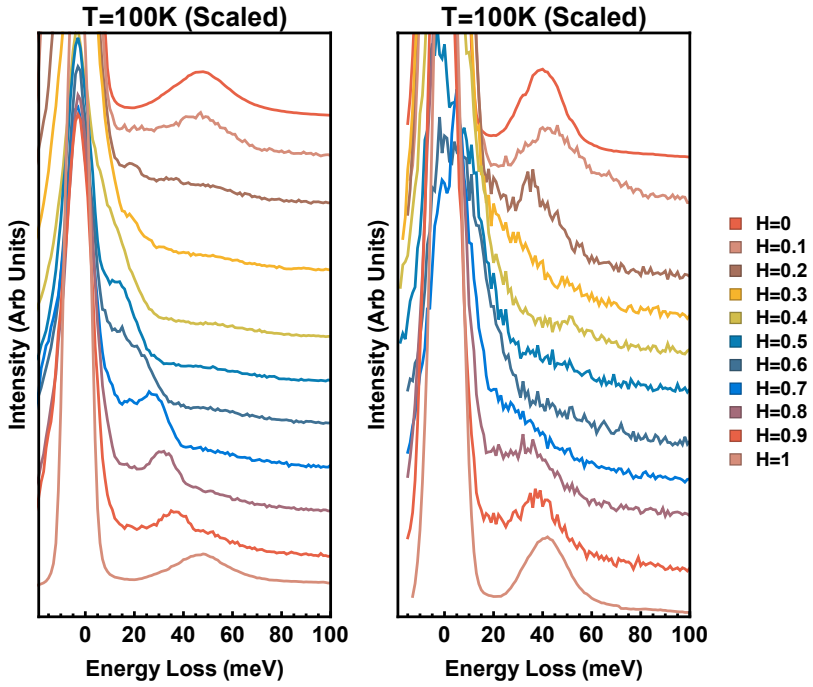

Figure 5.9: Raw M-EELS scans along (H,0) at 100 K for two different samples. The collection time per point for the plot on the left was twice as long as for the plot on the right.

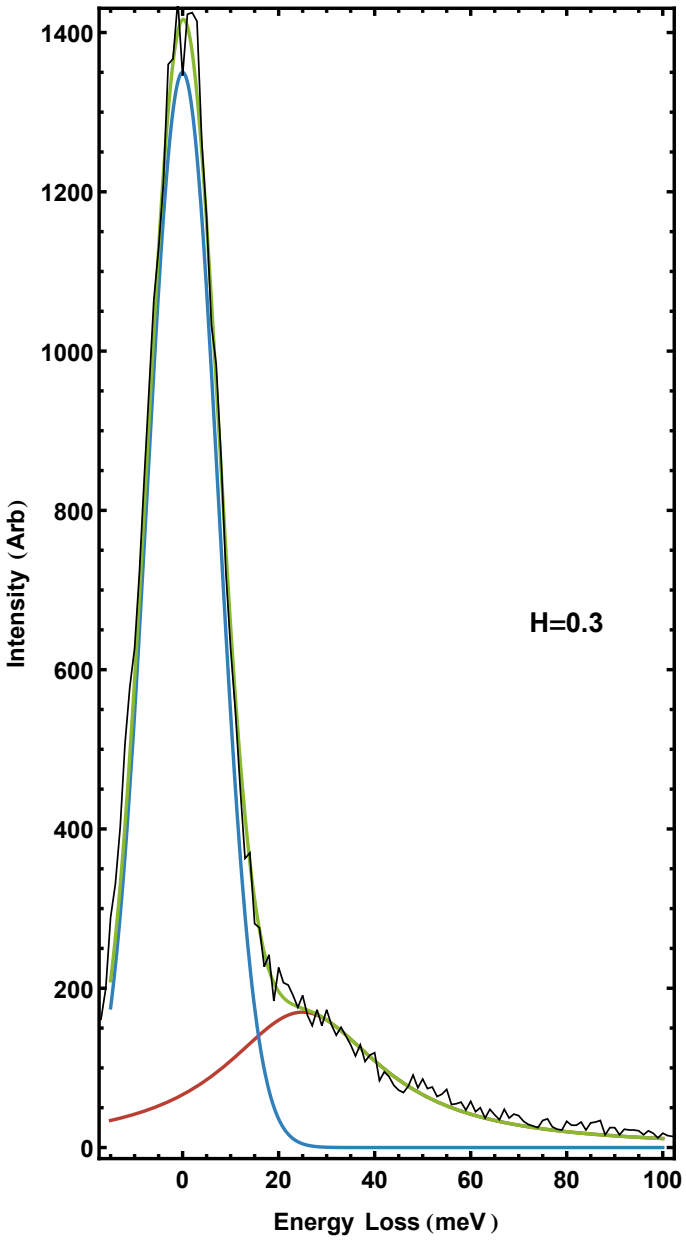

Figure 5.10: Example of fitting procedure showing an inelastic feature at ∼25 meV. The blue, red and green curves represent the fit to the elastic peak, the fit to the inelastic peak and the sum of the fits respectively. Scan was taken at H=0.3 and at T=100 K.

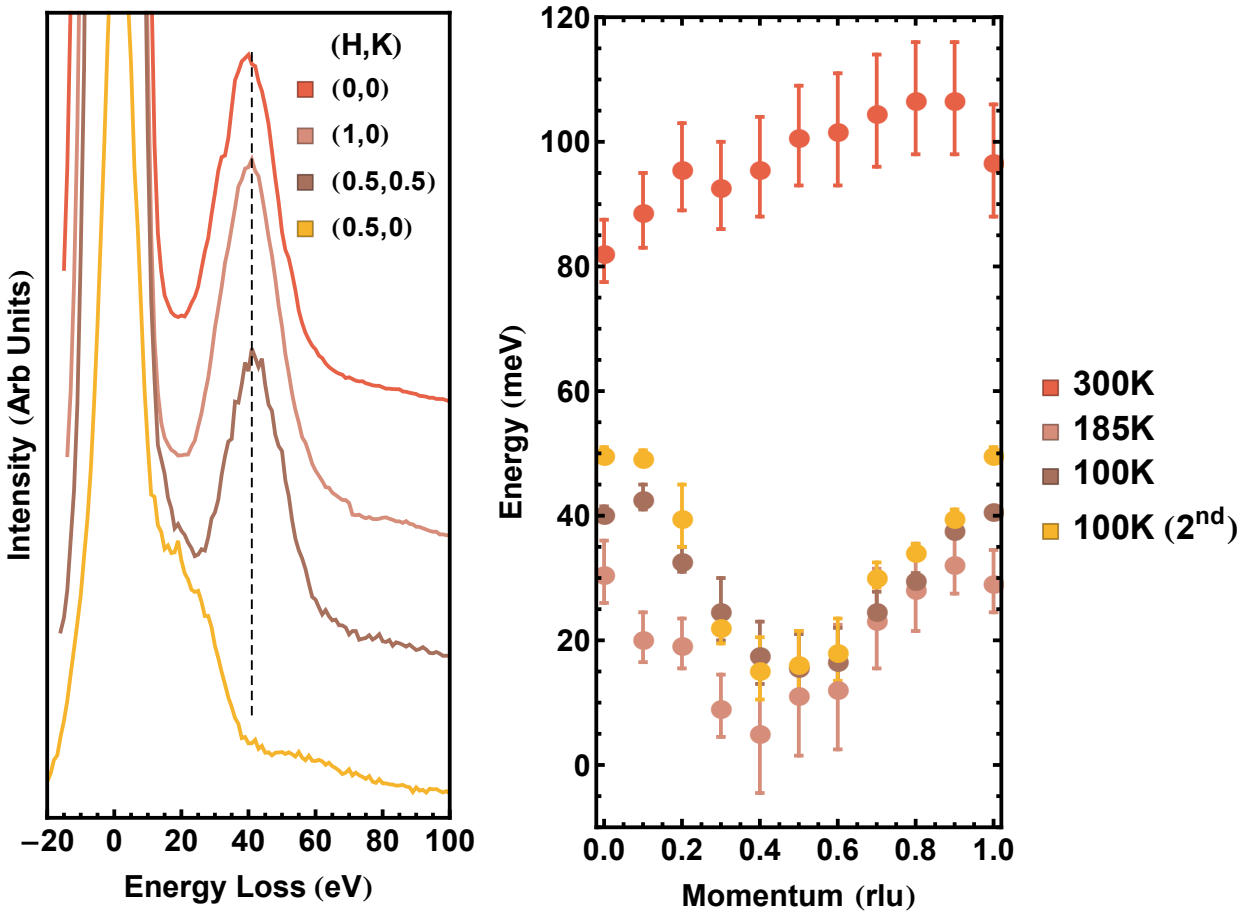

Figure 5.11: (Left) Inelastic spectra at Bragg points in the CDW phase. All spectra were taken at 100 K. (Right) Dispersion of collective modes at several different temperatures.

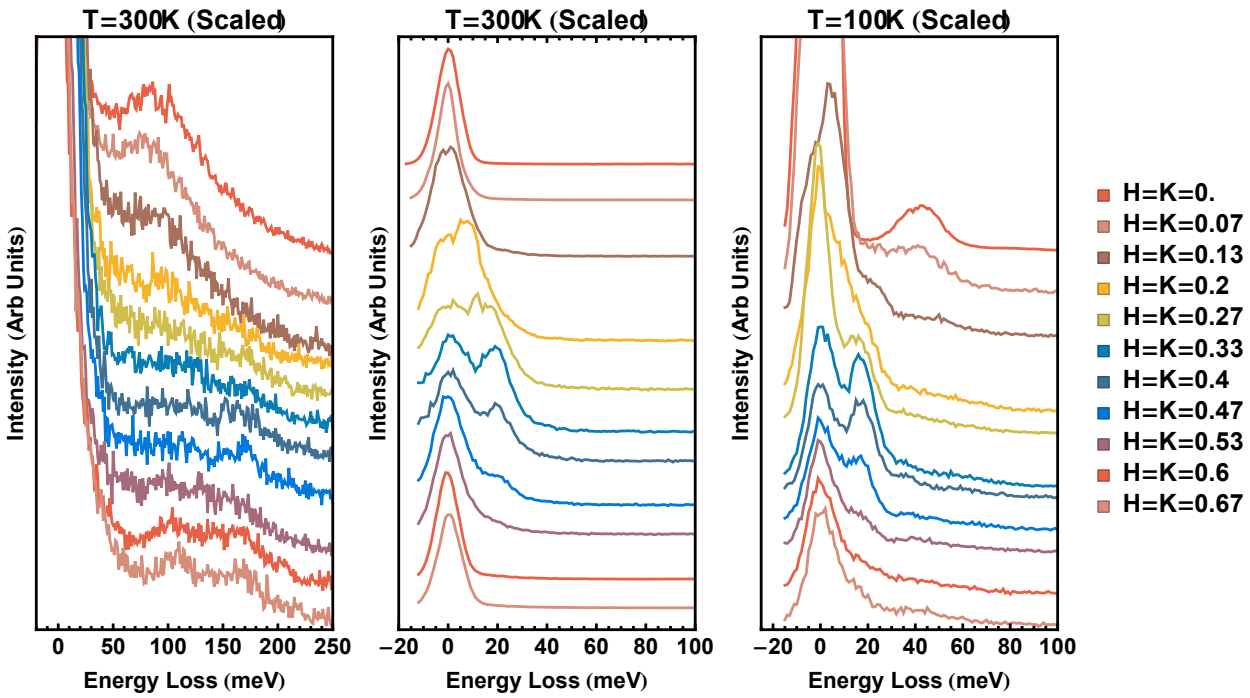

Figure 5.12: Raw M-EELS scans along (H,H) at 300 K and 100 K.

alluded to earlier.

5.2.2 Summary of Data Taken Along the (1,1) or $\Gamma \rightarrow K$ Direction

The data along the (1,1) direction are presented in Fig. 5.12 for T=300 K and T=100 K. Data were not taken at 185 K in this direction. There are a few features to note about the data in this direction as well. Firstly, the high energy mode, which is clearly visible at **q**=0, seems to damp away by about $\mathbf{q} \sim$ (0.2,0.2), while dispersing toward the elastic line. Moreover, there is a pronounced peak that emerges from the elastic peak at 100 K. This should be compared to the data at 300 K in the central panel of Fig. 5.12, where it is very clear that again an acoustic mode disperses out of the elastic peak. Also, it should be noted that the inelastic feature seen at 300 K at $\sim$ 85 meV disperses similarly to the peak in the (1,0) direction at 300 K. Clearly, the data along (1,1) contrast strongly to the data in the (1,0) direction below T_c.

5.3 Discussion and Interpretation

The natural first question to address concerning these data is the nature of the main high-energy excitation at $\mathbf{q} = 0$ (i.e. whether the mode is associated with the lattice or with the electronic degree of freedom). This can be answered by noting the following pieces of evidence: (1) Ref. [3] has shown that the observed excitation, both above and below T_c, gives rise to a noticeable plasma edge in the reflectivity spectrum as well as to a Drude tail in the optical conductivity; (2) Refs. [23], [75] and [79] have noted that there does not appear to be any lattice vibration with energy higher than $\sim$42 meV in $TiSe_2$, while well below T_c the observed mode resides at $\sim$50 meV; (3) since M-EELS is more sensitive to electronic modes, the strong intensity of this mode is highly suggestive of an electronic origin; and (4) because of the low carrier density in this compound, the free carrier plasmon is expected to reside in the 20-200 meV energy range [64]. Lastly, this mode went unobserved in inelastic X-ray studies, which are partial to lattice modes, again implying a strongly electronic character to this excitation. Put together, this body of evidence shows that the mode is of electronic origin (i.e. it is a conventional plasmon above T_c). With this knowledge, the dispersion of the mode in the critical region, shown in the right panel of Fig. 5.8, takes on added significance. It can be said that the plasmon appears to 'soften' near T_c at the CDW wavevector. This mode assignment, coupled with its dispersion near and below T_c provide strong evidence that the Coulomb interaction plays a prominent role in, and is likely the driving force behind, the transition to the CDW state in $TiSe_2$.

At present, the assignment of the acoustic mode in the (1,1) direction remains debatable. The high intensity of the feature again suggests an electronic origin to this mode, though the mode dispersion is also consistent with an acoustic phonon measured using inelastic neutron scattering (INS) in Ref. [80]. Because of this consistency, the mode is tentatively assigned to be an acoustic phonon, though it is suspected that there is an electronic component associated with this mode as well.

Below T_c, the electronic collective excitation may be regarded as a novel mode associated with the formation of the CDW/excitonic insulator phase. To corroborate this view, the dispersion of the collective mode below T_c exhibits an acoustic-like dispersion at the wavevector that connects the extrema of the normal-state conduction and valence bands. No such dispersion of the plasmon in seen in the normal state at 300 K. However, the collective mode below T_c is gapped at the CDW wavevector, which can be understood by noting that the CDW is commensurate. The other main piece of evidence supporting the identification of this mode as unconventional below T_c is the drastic dependence of the mode on temperature at $\mathbf{q}$=0. That the mode sharpens in linewidth and grows in intensity so dramatically with decreasing temperature is highly suggestive that the mode is closely associated with the low temperature CDW/excitonic insulator phase. Furthermore, the peak increases in energy with decreasing temperature, which is the opposite behavior one would expect of a normal plasmon in a low carrier concentration semiconducting compound. Usually, as the temperature is decreased, the number of thermal carriers is correspondingly reduced, leading to a lower plasma frequency. These observations, put together, are highly suggestive that the mode below T_c is the electronic counterpart to the phase mode commonly observed in more conventional electron-phonon coupled quasi-1D CDW materials [7]. Kohn has predicted the existence of such an electronic collective excitation in an excitonic insulator and has called it an "excitonic sound" wave [27].

5.4 Conclusion

The above evidence, including the observation of the softening of the plasmon at 185 K and of a novel electronic collective mode well below T_c associated with the excitonic condensate, provide the strongest affirmation to date that electron-electron interactions play a crucial role in the formation of the charge density wave state in $TiSe_2$. Taken together with the observation of a soft phonon in this material in Ref. [23], it can be said that both

the lattice and the electronic degrees of freedom are important in stabilizing the charge density wave in this material. The novel collective mode observed in this work should be contrasted to the usual phase mode observed in quasi-1D CDW materials, which is primarily of lattice character, but also possesses an electronic component [7]. Here, the mode is quite clearly of primarily electronic origin. Furthermore, with regard to the five criteria detailed above for the identification of the excitonic insulator state, it can now be said that the observations made in this work are consistent with and strongly suggestive of the idea that $TiSe_2$ is indeed an excitionic insulator. This claim implies that plasmon-phonon mixing must occur in a resolution window beyond the capability of our instrument, and provides a direction for future experiments. The results seen here moreover bear a striking resemblance to those theoretically predicted by Kohn in Ref. [27] with regard to the excitonic insulator phase in semimetallic compounds. Therefore, $TiSe_2$ may be, at present, the first material convincingly shown to undergo a transition to an excitonic insulator state in a solid-state setting. The collective mode at $\sim$50 meV at $\mathbf{q} = 0$, observed well below T_c, therefore constitutes the observation of an "excitonic sound" wave associated with the excitonic insulator condensate.

Chapter 6

Conclusion

In this thesis, the development of a goniometer to provide an electron energy-loss spectrometer with true momentum space mapping was undertaken. Furthermore, the improvement of a theoretical framework with which to understand the M-EELS cross section was worked out within a context provided by Ref. [31]. These methods were applied to comprehend the ARPES quasiparticle dispersion anomalies, whose origins have been speculated upon for at least a decade, in several different materials. Lastly, compelling evidence for the existence of the excitonic insulator ground state in $TiSe_2$, deduced through unusual plasmon dynamics and the observation of a novel collective mode, was presented. These facts, supplemented by the experimental observations made by others, provide the strongest affirmation for the existence of the excitonic insulator state in a solid-state setting to date.

References

[1] Tu, J., Homes, C., Gu, G., and Strongin, M. Physica B: Condensed Matter **316**, 324–327 (2002).

[2] Nücker, N., Romberg, H., Nakai, S., Scheerer, B., Fink, J., Yan, Y. F., and Zhao, Z. X. Phys. Rev. B **39**, 12379–12382 Jun (1989).

[3] Li, G., Hu, W. Z., Qian, D., Hsieh, D., Hasan, M. Z., Morosan, E., Cava, R. J., and Wang, N. L. Phys. Rev. Lett. **99**, 027404 Jul (2007).

[4] Laughlin, R. B. and Pines, D. Proceedings of the National Academy of Sciences **97**(1), 28–31 (2000).

[5] Ashcroft, N. and Mermin, N. Solid State Physics. Saunders College, Philadelphia, (1976).

[6] Ziman, J. Principles of the Theory of Solids. Cambridge University Press, London, England, (1964).

[7] Gruner, G. Density Waves in Solids. Addison-Wesley, (1994).

[8] Nozieres, P. and Pines, D. Theory Of Quantum Liquids. Advanced Books Classics Series. Westview Press, (1999).

[9] Als-Nielsen, J. and McMorrow, D. Elements of Modern X-ray Physics. Wiley, (2011).

[10] Krivanek, O. L., Lovejoy, T. C., Murfitt, M. F., Skone, G., Batson, P. E., and Dellby, N. Journal of Physics: Conference Series **522**(1), 012023 (2014).

[11] Krivanek, O. L., Lovejoy, T. C., Dellby, N., Aoki, T., Carpenter, R., Rez, P., Soignard, E., Zhu, J., Batson, P. E., Lagos, M. J., et al. Nature **514**(7521), 209–212 (2014).

[12] Johannes, M. D. and Mazin, I. I. Phys. Rev. B **77**, 165135 Apr (2008).

[13] Valla, T., Fedorov, A. V., Johnson, P. D., Xue, J., Smith, K. E., and DiSalvo, F. J. Phys. Rev. Lett. **85**, 4759–4762 Nov (2000).

[14] Leggett, A. J. Proceedings of the National Academy of Sciences **96**(15), 8365–8372 (1999).

[15] Leggett, A. J. Journal of Physics and Chemistry of Solids **59**(10), 1729–1732 (1998).

[16] Ginzburg, V. Annu. Rev. Mater. Sci. **2**, 663 – 696 (1972).

[17] Zaanen, J., Chakravarty, S., Senthil, T., Anderson, P., Lee, P., Schmalian, J., Imada, M., Pines, D., Randeria, M., Varma, C., et al. Nature Physics **2**(3), 138–143 (2006).

[18] Raghu, S., Chung, S. B., Qi, X.-L., and Zhang, S.-C. Phys. Rev. Lett. **104**, 116401 Mar (2010).

[19] Yang, H.-B., Pan, Z.-H., Sekharan, A. K. P., Sato, T., Souma, S., Takahashi, T., Jin, R., Sales, B. C., Mandrus, D., Fedorov, A. V., Wang, Z., and Ding, H. Phys. Rev. Lett. **95**, 146401 Sep (2005).

[20] Valla, T., Fedorov, A. V., Johnson, P. D., and Hulbert, S. L. Phys. Rev. Lett. **83**, 2085–2088 Sep (1999).

[21] Schäfer, J., Schrupp, D., Rotenberg, E., Rossnagel, K., Koh, H., Blaha, P., and Claessen, R. Phys. Rev. Lett. **92**, 097205 Mar (2004).

[22] Weber, F., Rosenkranz, S., Castellan, J.-P., Osborn, R., Hott, R., Heid, R., Bohnen, K.-P., Egami, T., Said, A. H., and Reznik, D. Phys. Rev. Lett. **107**, 107403 Sep (2011).

[23] Weber, F., Rosenkranz, S., Castellan, J.-P., Osborn, R., Karapetrov, G., Hott, R., Heid, R., Bohnen, K.-P., and Alatas, A. Phys. Rev. Lett. **107**, 266401 Dec (2011).

[24] Zhu, X., Cao, Y., Zhang, J., Plummer, E. W., and Guo, J. Proceedings of the National Academy of Sciences **112**(8), 2367–2371 (2015).

[25] Rossnagel, K. Journal of Physics: Condensed Matter **23**(21), 213001 (2011).

[26] Borisenko, S. V., Kordyuk, A. A., Yaresko, A. N., Zabolotnyy, V. B., Inosov, D. S., Schuster, R., Büchner, B., Weber, R., Follath, R., Patthey, L., and Berger, H. Phys. Rev. Lett. **100**, 196402 May (2008).

[27] Kohn, W. In Many-Body Physics, DeWitt, C. and Balian, R., editors. Gordon and Breach (1968).

[28] Van Hove, L. Phys. Rev. **95**, 249–262 Jul (1954).

[29] Sakurai, J. J. Modern Quantum Mechanics (Revised Edition). Addison Wesley, 1 edition, September (1993).

[30] Ibach, H. and Mills, D. L. Electron Energy Loss Spectroscopy and Surface Vibrations. Academic Press, (1982).

[31] Evans, E. and Mills, D. L. Phys. Rev. B **5**, 4126 (1972).

[32] Ormeci, A., Hall, B. M., and Mills, D. L. Phys. Rev. B **42**, 4524 (1990).

[33] Pines, D. Elementary Excitations in Solids: Lectures on Protons, Electrons, and Plasmons. Advanced book classics. Perseus Books, (1999).

[34] Mills, D. L. Surface Science **48**, 59 (1975).

[35] Ibach, H. Phys. Rev. Lett. **24**, 1416–1418 (1970).

[36] Ibach, H. Electron Energy Loss Spectrometers: The Technology of High Performance. Springer series in optical sciences. Springer-Verlag, (1991).

[37] Damascelli, A. Physica Scripta **2004**(T109), 61 (2004).

[38] Lanzara, A., Bogdanov, P., Zhou, X., Kellar, S., Feng, D., Lu, E., Yoshida, T., Eisaki, H., Fujimori, A., Kishio, K., et al. Nature **412**(6846), 510–514 (2001).

[39] Kondo, T., Nakashima, Y., Ota, Y., Ishida, Y., Malaeb, W., Okazaki, K., Shin, S., Kriener, M., Sasaki, S., Segawa, K., and Ando, Y. Phys. Rev. Lett. **110**, 217601 May (2013).

[40] Chen, C., Xie, Z., Feng, Y., Yi, H., Liang, A., He, S., Mou, D., He, J., Peng, Y., Liu, X., et al. Scientific reports **3** (2013).

[41] Wray, L. A., Xu, S.-Y., Xia, Y., San Hor, Y., Qian, D., Fedorov, A. V., Lin, H., Bansil, A., Cava, R. J., and Hasan, M. Z. Nature Physics **6**(11), 855–859 (2010).

[42] Wollman, D. A., Van Harlingen, D. J., Giapintzakis, J., and Ginsberg, D. M. Phys. Rev. Lett. **74**, 797–800 Jan (1995).

[43] Valla, T., Fedorov, A., Johnson, P., Wells, B., Hulbert, S., Li, Q., Gu, G., and Koshizuka, N. Science **285**(5436), 2110–2113 (1999).

[44] Cuk, T., Baumberger, F., Lu, D. H., Ingle, N., Zhou, X. J., Eisaki, H., Kaneko, N., Hussain, Z., Devereaux, T. P., Nagaosa, N., and Shen, Z.-X. Phys. Rev. Lett. **93**, 117003 Sep (2004).

[45] Devereaux, T. P., Cuk, T., Shen, Z.-X., and Nagaosa, N. Phys. Rev. Lett. **93**, 117004 Sep (2004).

[46] Norman, M. R., Randeria, M., Ding, H., and Campuzano, J. C. Phys. Rev. B **52**, 615–622 Jul (1995).

[47] Vig, S., Kogar, A., Mishra, V., Venema, L., Cartonlano, M., Huasin, A., Gu, G., Fradkin, E., Norman, M., and Abbamonte, P. To be published .

[48] Vishik, I. M., Lee, W. S., Schmitt, F., Moritz, B., Sasagawa, T., Uchida, S., Fujita, K., Ishida, S., Zhang, C., Devereaux, T. P., and Shen, Z. X. Phys. Rev. Lett. **104**, 207002 May (2010).

[49] Kordyuk, A. A., Borisenko, S. V., Knupfer, M., and Fink, J. Phys. Rev. B **67**, 064504 Feb (2003).

[50] Kane, C. L. and Mele, E. J. Physical review letters **95**(14), 146802 (2005).

[51] Bernevig, B. A., Hughes, T. L., and Zhang, S.-C. Science **314**(5806), 1757–1761 (2006).

[52] König, M., Wiedmann, S., Brüne, C., Roth, A., Buhmann, H., Molenkamp, L. W., Qi, X.-L., and Zhang, S.-C. Science **318**(5851), 766–770 (2007).

[53] Fu, L., Kane, C. L., and Mele, E. J. Phys. Rev. Lett. **98**, 106803 Mar (2007).

[54] Zhang, H., Liu, C.-X., Qi, X.-L., Dai, X., Fang, Z., and Zhang, S.-C. Nature physics **5**(6), 438–442 (2009).

[55] Hsieh, D., Xia, Y., Qian, D., Wray, L., Dil, J., Meier, F., Osterwalder, J., Patthey, L., Checkelsky, J., Ong, N., et al. Nature **460**(7259), 1101–1105 (2009).

[56] Analytis, J. G., Chu, J.-H., Chen, Y., Corredor, F., McDonald, R. D., Shen, Z. X., and Fisher, I. R. Phys. Rev. B **81**, 205407 May (2010).

[57] Economou, E. N. Phys. Rev. **182**, 539–554 Jun (1969).

[58] Egdell, R., Evans, S., Stradling, R., Li, Y., Parker, S., and Williams, R. Surface Science **262**(3), 444 – 450 (1992).

[59] Richter, W. and Becker, C. R. physica status solidi (b) **84**(2), 619–628 (1977).

[60] Stordeur, M., Ketavong, K. K., Priemuth, A., Sobotta, H., and Riede, V. physica status solidi (b) **169**(2), 505–514 (1992).

[61] Sushkov, A. B., Jenkins, G. S., Schmadel, D. C., Butch, N. P., Paglione, J., and Drew, H. D. Phys. Rev. B **82**, 125110 Sep (2010).

[62] Wray, L. A. Spectroscopic studies of unconventional superconductivity in iron pnictides and doped topological insulators. PhD thesis, Princeton University, (2010).

[63] The smaller restoring force accounts for the slight discrepancy in energy of this mode compared to bulk probes, as it oscillates out of the plane at the surface.

[64] Di Salvo, F. J., Moncton, D. E., and Waszczak, J. V. Phys. Rev. B **14**, 4321–4328 Nov (1976).

[65] Moncton, D. E., Axe, J. D., and DiSalvo, F. J. Phys. Rev. B **16**, 801–819 Jul (1977).

[66] Sipos, B., Kusmartseva, A. F., Akrap, A., Berger, H., Forró, L., and Tutiš, E. Nature materials **7**(12), 960–965 (2008).

[67] Kidd, T. E., Miller, T., Chou, M. Y., and Chiang, T.-C. Phys. Rev. Lett. **88**, 226402 May (2002).

[68] Rasch, J. C. E., Stemmler, T., Müller, B., Dudy, L., and Manzke, R. Phys. Rev. Lett. **101**, 237602 Dec (2008).

[69] Rohwer, T., Hellmann, S., Wiesenmayer, M., Sohrt, C., Stange, A., Slomski, B., Carr, A., Liu, Y., Avila, L. M., Kalläne, M., et al. Nature **471**(7339), 490–493 (2011).

[70] van Wezel, J., Nahai-Williamson, P., and Saxena, S. S. Phys. Rev. B **81**, 165109 Apr (2010).

[71] Hellmann, S., Rohwer, T., Kalläne, M., Hanff, K., Sohrt, C., Stange, A., Carr, A., Murnane, M., Kapteyn, H., Kipp, L., et al. Nature communications **3**, 1069 (2012).

[72] Cercellier, H., Monney, C., Clerc, F., Battaglia, C., Despont, L., Garnier, M. G., Beck, H., Aebi, P., Patthey, L., Berger, H., and Forró, L. Phys. Rev. Lett. **99**, 146403 Oct (2007).

[73] Jérome, D., Rice, T. M., and Kohn, W. Phys. Rev. **158**, 462–475 Jun (1967).

[74] Mott, N. F. Philosophical Magazine **6**, 287–309 February (1961).

[75] Holt, M., Zschack, P., Hong, H., Chou, M. Y., and Chiang, T.-C. Phys. Rev. Lett. **86**, 3799–3802 Apr (2001).

[76] Rossnagel, K., Kipp, L., and Skibowski, M. Phys. Rev. B **65**, 235101 May (2002).

[77] Porer, M., Leierseder, U., Ménard, J.-M., Dachraoui, H., Mouchliadis, L., Perakis, I., Heinzmann, U., Demsar, J., Rossnagel, K., and Huber, R. Nature materials **13**(9), 857–861 (2014).

[78] Snow, C. S., Karpus, J. F., Cooper, S. L., Kidd, T. E., and Chiang, T.-C. Phys. Rev. Lett. **91**, 136402 Sep (2003).

[79] Holy, J. A., Woo, K. C., Klein, M. V., and Brown, F. C. Phys. Rev. B **16**, 3628–3637 Oct (1977).

[80] Stirling, W., Dorner, B., Cheeke, J., and Revelli, J. Solid State Communications **18**(7), 931 – 933 (1976).